



저작자표시-동일조건변경허락 2.0 대한민국

이용자는 아래의 조건을 따르는 경우에 한하여 자유롭게

- 이 저작물을 복제, 배포, 전송, 전시, 공연 및 방송할 수 있습니다.
- 이차적 저작물을 작성할 수 있습니다.
- 이 저작물을 영리 목적으로 이용할 수 있습니다.

다음과 같은 조건을 따라야 합니다:



저작자표시. 귀하는 원저작자를 표시하여야 합니다.



동일조건변경허락. 귀하가 이 저작물을 개작, 변형 또는 가공했을 경우에는, 이 저작물과 동일한 이용허락조건하에서만 배포할 수 있습니다.

- 귀하는, 이 저작물의 재이용이나 배포의 경우, 이 저작물에 적용된 이용허락조건을 명확하게 나타내어야 합니다.
- 저작권자로부터 별도의 허가를 받으면 이러한 조건들은 적용되지 않습니다.

저작권법에 따른 이용자의 권리는 위의 내용에 의하여 영향을 받지 않습니다.

이것은 [이용허락규약\(Legal Code\)](#)을 이해하기 쉽게 요약한 것입니다.

[Disclaimer](#)

공학석사학위논문

**Development of a Vector Following Mesh  
Generator for Analysis of Two Dimensional  
Tokamak Plasma Transport**

2차원 토카막 플라즈마 수송을 위한

벡터 추적 메쉬 생성기의 개발

2014년 2월

서울대학교 대학원

에너지시스템공학부

김 영 진



**Development of a Vector Following Mesh  
Generator for Analysis of Two Dimensional  
Tokamak Plasma Transport**

2차원 토카막 플라즈마 수송을 위한  
벡터 추적 메쉬 생성기의 개발

지도 교수 나 용 수

이 논문을 공학석사 학위논문으로 제출함  
2014년 2월

서울대학교 대학원  
에너지시스템공학부  
김 영 진

김영진의 공학석사 학위논문을 인준함  
2014년 2월

위 원 장 황 용 석 (인)

부위원장 나 용 수 (인)

위 원 전 영 무 (인)





# Abstract

## Development of a Vector Following Mesh Generator for Analysis of Two Dimensional Tokamak Plasma Transport

Kim, Youngjin

Department of Energy Systems Engineering  
Seoul National University

A time-varying adaptive grid is required for multi-dimensional, time-dependent transport modeling of tokamak plasmas where the plasma equilibrium evolves according to plasma transport. In addition, a spatially inhomogeneous adaptive grid is needed for integrated transport modeling of different spatial scales. A number of mesh generators have been developed to provide calculation domains for two dimensional transport analyses mainly focused on the SOL-private region. However, generally these conventional mesh generators give a time-invariant grid without further updating during whole simulations. Therefore, these codes are unfavorable to simulate phenomena, where plasma properties vary significantly in time and space so that requiring continuous update of spatially inhomogeneous grids, appearing in the L-mode to H-mode transition, Edge Localized Modes (ELMs), and so on.

A new adaptive mesh generator is developed in this thesis for 2-D core-

edge coupled transport simulations specified for plasma conditions where the plasma configuration is rather fixed but internal equilibrium is still dynamically varying. The geometric mesh type of the field aligned orthogonal structured mesh is employed appropriate for the Finite Volume Method (FVM) which decomposes the parallel and the radial direction to the magnetic field due to strong anisotropy of transport in a magnetized plasma. Thus, the mesh is created orthogonally based on the poloidal magnetic field map of given boundary equilibrium profiles suitable for both Single Null (SN) and Double Null (DN) divertor configurations. It is also developed to attain flexibility in generating grid distributions for optimizing calculation domains according to various plasma phenomena which one focuses in transport modeling. The mesh generator can generate spatially non-uniform grids by considering different spatial scales when treating global and highly localized phenomena simultaneously.

In general, because there is no transformation relation between the plasma transport equation and the discretization equation, the mesh generation is operated by algebraic assumptions like an interpolation scheme. In this condition, the vector following method is introduced to find a desired position by using information of the poloidal magnetic field map.

The newly developed mesh generator is evaluated in three way. Firstly, it is applied to produce a mesh for a KSTAR geometry where the plasma equilibrium is taken from the Tokamak Equilibrium Solver (TES) code. The property of the generated mesh is evaluated in a quantitative way by introducing some mesh quality factors based on a criterion of the flux

conservation in the FVM method.

Secondly, the mesh generator is verified with a conventional code, CARRE in terms of the mesh quality factors. It is found that the numerical results are generally similar between them but an improvement in the private region is detected in the newly developed code near the divertor region. Furthermore, the radial flux error at the separatrix lines is more alleviated than the CARRE code, which is more desirable to simulate plasma boundary physics such as Multifaceted Asymmetric Radiation From the Edge (MARFE) and ELMs.

Thirdly, the capability of the non-uniform grid generation is evaluated. Non-uniform grids are produced in the core region in two ways. One is generated by considering the ion Larmor radius and the other by considering local steep gradients such as transport barriers. They are compared with a reference case with uniform distribution. A more refined grid is found near the edge region characterized with smaller ion Larmor radius and steeper gradient whereas coarser one in the core. Such fine grid at the edge region is indeed suitable for analysis of edge-SOL transport.

The developed vector following mesh generator in this thesis will deal with adaptable meshes changing with time according to the equilibrium evolution by directly connected with the transport solver for coupled time-dependent core-edge SOL simulations.

**Keywords:** adaptive grid, orthogonal mesh, vector following method, automatic non-uniform grid generation, two dimensional

tokamak transport, FVM discretization, mesh quality, numerical  
code

**Student Number: 2012-20993**

## Contents

<b>Abstract</b>	<b>i</b>
<b>Contents</b>	<b>v</b>
<b>List of Tables</b>	<b>vii</b>
<b>List of Figures</b>	<b>viii</b>
<b>Chapter 1 Introduction</b>	<b>1</b>
1.1 Two dimensional modeling for tokamak plasmas	1
1.2 Review of conventional mesh generators	2
1.3 Objective and scope of this numerical work	3
<b>Chapter 2 Description of Mesh Generator for 2-D Tokamak Plasmas</b>	<b>5</b>
2.1 Mesh criterion for 2-D tokamak modeling	6
2.1.1 Field alignment	8
2.1.2 Orthogonality	9
2.1.3 Adaptivity	11
2.2 Specification of the mesh generator development	12
2.2.1 Magnetic coordinate	14
2.2.2 Magnetic field configurations	16
<b>Chapter 3 Vector Following Orthogonal Mesh Generation</b>	<b>18</b>
3.1 Methodology of orthogonal mesh generation	18
3.1.1 Vector following method	18
3.1.2 Definition of the magnetic field configurations	22
3.1.3 Non-uniform grid generations	25
3.1.4 Normal vector tracing	30
3.2 Numerical procedure	32
<b>Chapter 4 Verification of the Developed Code</b>	<b>35</b>
4.1 Initial conditions for the reference mesh generation	36
4.1.1 Grid refinement of non-uniform grid distribution	36
4.1.2 Initial distribution shapes of diverted plasmas	37

4.2	Evaluation of the mesh quality .....	41
4.2.1	Quality factor .....	42
4.2.2	Measurement of mesh quality for the reference distribution	43
4.3	Benchmarking with the CARRE code .....	46
<b>Chapter 5</b>	<b>Automatic Non-uniform Grid Generation .....</b>	<b>56</b>
5.1	Input profile for the core distributions .....	56
5.1.1	Stationary mode .....	56
5.1.2	Subdomain mode .....	58
5.2	Comparison with the reference distribution .....	59
<b>Chapter 6</b>	<b>Conclusions.....</b>	<b>65</b>
<b>Bibliography.....</b>		<b>67</b>
<b>국문초록</b>	<b>69</b>	

## List of Tables

Table 2.1	Classification of possible magnetic configurations for diverted plasma and conventions.....	16
Table 4.1	Reference grid distribution parameter of the stretching function at each regions for the KSTAR double null configuration.....	37
Table 4.2	Initial grid node numbers of KSTAR double null configurations for the reference mesh generation .....	40
Table 5.1	Distribution of subdomain mode in the core region.....	58

# List of Figures

Figure 2.1 Schematic view of typical tokamak plasma.....	6
Figure 2.2 Control volume used in the FVM discretization .....	10
Figure 2.3 Magnetic coordinate system for the FVM discretization .....	15
Figure 2.4 Schematic representation of the magnetic field configurations ....	17
Figure 3.1 Flow chart of the vector following method. ....	21
Figure 3.2 Schematic view of the magnetic field configuration and poloidal magnetic field direction in the double null configuration .....	25
Figure 3.3 Nodal distribution on one line and effects of $E, D$ , and $S$ .....	27
Figure 3.4 Two constraints during the normal vector tracing .....	31
Figure 4.1 Initial equilibrium from the TES code of the KSTAR double null configuration.....	39
Figure 4.2 The result of the constructed mesh of the various KSTAR configurations	40
Figure 4.3 Schematic diagram of a control volume for discretization in FVM and deviation.....	41
Figure 4.4 Contour plots of the average quantities of cell orthogonality and radial flux deviation at each regions for the reference double null configuration.....	44
Figure 4.5 Radial variations of standard deviation of $\psi$ at each regions for the reference double null configuration.....	45
Figure 4.6 Comparison of the averaged quantity of deviation parameters from an ideal orthogonal mesh in the reference double null configuration .....	48
Figure 4.7 Variations of deviation parameters in the private regions (region 2, 4) along the (a) radial and (b) poloidal direction .....	50
Figure 4.8 Variations of deviation parameters in the core region (region 5) along the (a) radial and (b) poloidal direction. ....	51
Figure 4.9 Poloidal variations of flux deviation in the core region (region 5) at	

	the each flux surface in the vicinity of the edge region. n refers radial node number.....	52
Figure 4.10	Comparison of the average value of flux deviation at each separatrix lines (1 : upper right, 2 : upper left, 3: lower right, 4 : lower left, 5 : outer core, 6 : inner core) which are computed by the vector following method (red) and CARRE (blue) code, respectively.....	54
Figure 4.11	Radial flux deviations at each separatrix lines along the poloidal direction: (a) divertor separatrix and (b) core separatrix, which are computed by the vector following method (red) and CARRE (blue) code, respectively.....	55
Figure 5.1	One dimensional radial ion temperature profile by the shape function in the core region for stationary mode.....	57
Figure 5.2	Radial distribution of the subdomain mode in the core region.....	59
Figure 5.3	Core distribution shapes of various operation mode: uniform distribution (blue), stationary mode (green) and subdomain mode (magenta), respectively .....	60
Figure 5.4	Comparison of the averaged quantity of deviation parameters: (a) cell orthogonality (b) radial flux deviation from an ideal orthogonal mesh in the various core distributions.....	61
Figure 5.5	Poloidal variations of (a) cell orthogonality and (b) radial flux deviation in the core region (region 5) for the various core distributions at the each flux surface from n = 2 to n = 4. n refers radial node number.....	63
Figure 5.6	Radial flux deviations at the core separatrix lines for the various core distributions: (a) total average value and (b) poloidal scan ..	64

# Chapter 1

## Introduction

### 1.1 Two dimensional modeling for tokamak plasmas

Recent progress of a tokamak plasma simulation in a time dependent situation enables a core-edge-SOL coupled problem because a plasma boundary phenomena such as Edge Localized Modes (ELMs), L-H transitions and impurity puffs strongly influences a global confinement performance [1]. The simultaneous simulation of whole regions has advantage of providing a consistency check on the boundary conditions and on the results of the individual simulations. In addition, a global code can offer a new physics tool that allows the study of the interplay of core and edge processes that are experimentally difficult to separate.

There are two possibilities of extending code to either couple them to a core code at a specified interface (1.5-D/2-D) or to extend the computational region of an SOL-code all the way to the plasma center (2-D). The advantages of the latter strategy are that it leads to a homogenous code and avoids the need of an interface between core and edge. Furthermore poloidal asymmetries of heavier impurities in the core could in principle be resolved [1]. The main drawback is that the separation of core and edge time scales is difficult. But recent progress in computational resources has made advanced

two dimensional simulation of tokamak plasmas feasible using a parallel computation [2, 3]. In a situation when two dimensional transport is extended to the entire regions, two dimensional mesh could provide a numerical calculation domain to solve core-edge coupled transport. Therefore, an accurate mesh construction is essential before transport analysis.

## **1.2 Review of conventional mesh generators**

A number of two dimensional mesh generator have been developed for two dimensional tokamak plasma simulations. But established mesh generators are intended to focusing only a SOL or edge-SOL region due to the difference in topology and time scales between the core and SOL region. One of the famous mesh code for the edge simulation is CARRE [4] which is widely used for the edge-SOL code such as SOLPS [5], UEDGE [6] and C2 [2]. It generates a logically rectangular curvilinear quadrilateral field-aligned grid for a divertor modeling. After an orthogonal mesh is constructed, SOL simulations are well conducted onto a static grid to analyze local and qualitative edge physics such as a heat flux calculation, ELMs and Multifaceted Asymmetric Radiation From the Edge (MARFE) in a short time scale ( $\sim$  ms). But the static mesh is generated only once and fixed during entire simulations, it has problems when considering plasma equilibrium evolving for global simulations [7]. In the edge region,

especially, the plasma equilibrium is rapidly varying due to the core profile change such as a confinement mode transition, neutral fueling, impurity seeding, auxiliary heating and so on. Therefore, the mesh must represent correctly the real plasma configuration to conserve advantage of the two dimensional modeling. In addition, the computational mesh is made nearly orthogonally in accordance with geometrical shapes of a plasma. It is not considered physical property of each regions. For example, the core-edge mesh is constructed all together not considering two region separately whose method requires additional data converting to determine such as the pedestal width for an analysis of edge region phenomena.

Practical usage of existing mesh codes has a problem as well. The mesh is built only once initially, so the input data for mesh creation is transferred by user's passive selecting. This results additional data pre-processing and converting are needed before transport simulations, which is a complex numerical procedure and time consuming. Therefore, once the mesh is produced initially, automatic mesh generation linked with plasma parameters is needed.

### **1.3 Objective and scope of this numerical work**

For the above reasons, the objective in this thesis is the development of a new mesh generator which is more optimized to integrate with a plasma transport solver for core-edge coupled simulations and more flexible than the conventional edge mesh generation codes. This code can be applicable to a

2-D core-edge coupled transport simulations where the plasma configuration is rather fixed but internal equilibrium is still evolving with time, thus the mesh is generated with time in the core region to represent an equilibrium evolving. This plasma condition is associated with the plasma current flat-top phase in the tokamak operation. The geometric mesh type of this works is a field-aligned orthogonal structured mesh for using the FVM discretization of a transport equation. A non-uniform grid distribution is available initially by user's interest using the grid distribution function. However, the core-edge mesh distributions can be varied automatically in each transport iterations considering physical parameters on various simulation purposes. No passive input data are required in this process because distribution parameters in the core region to mapping domain are intended to directly link with the transport code. The developed mesh generator is invented to improve simulations for edge physics such as the mode transition, ELMs and poloidal asymmetric situation, which is more promising for the adaptive grid concept.

## **Chapter 2**

### **Description of Mesh Generator for 2-D**

#### **Tokamak Plasmas**

As shown in a schematic view in Figure 2.1, the tokamak plasma can be divided into three regions; core, edge, and SOL. In the core region, particles and energy of plasma are well confined due to the closed magnetic field configurations. In the SOL region, On the other hand, the magnetic field lines intersect with the material surfaces of plasma facing components (PFCs) such as divertor plates, limiter and first wall segments, so that it is important to compute the transport not only across the magnetic flux surfaces but also along the magnetic field lines. This magnetic topology of the tokamak makes different transport characteristics of the two regions but some of transport parameters interact each other simultaneously at the edge (or pedestal) region.

The majority of 2-D models of tokamak plasma are based on the Braginskii's equation, since it describes the behavior of magnetized plasmas in a simple form [8]. To perform the coupled transport simulation in the entire tokamak regions successfully with reducing a computational time, the parallel computation is useful that divides the entire domain into several subdomains.

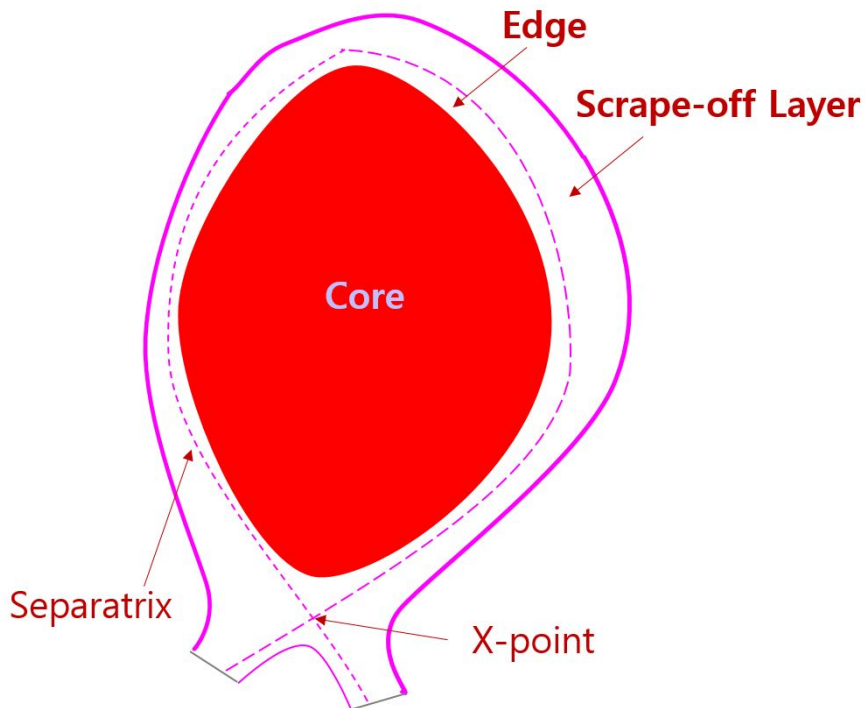


Figure 2.1 Schematic view of typical tokamak plasma

## 2.1 Mesh criterion for 2-D tokamak modeling

In a fluid description of a plasma, physical aspects of any fluid flow are governed by fundamental principles of conservation law. These principles can be expressed in terms of mathematical equations, which are usually Partial Differential Equations (PDEs). But the main difficulty of 2-D plasma transport modeling arises from that magnetic field. This causes a strong anisotropy in plasma properties due to fast streaming of charged particles along the field line but preventing the plasma transport across the magnetic

surfaces.

In a situation to solve PDEs numerically based on a fluid plasma, Finite Volume Method (FVM) provides a simple way of discretization without the need to introduce generalized coordinates. It is also supported by situations, where the conservation laws cannot be represented by PDEs but only the integral forms are guaranteed. Furthermore, being based on the conservative form, it naturally satisfies the divergence free condition of magnetic field [9]. For these reasons, FVM has been successful in the majority of numerical models for the 2-D edge/SOL fluid codes such as B2, UEDGE, and C2.

In the FVM, volume integrals in a PDEs that contain a divergence term are converted to surface integrals, using the divergence theorem. These terms are then evaluated as fluxes at the surfaces of each finite volume.

$$\int dV \nabla \cdot \vec{F} = \int \vec{F} \cdot d\vec{A} = \vec{F}_e \cdot d\vec{A}_e + \vec{F}_w \cdot d\vec{A}_w + \vec{F}_n \cdot d\vec{A}_n + \vec{F}_s \cdot d\vec{A}_s \quad (2.1)$$

Because a flux entering a given volume is identical to that leaving the adjacent volume, these methods are conservative.

To solve FVM discretized equations numerically, a curvilinear mesh that provides a computational domain is required. If the mesh cannot denote magnetic configurations when a plasma is highly magnetized, calculation results has low accuracy and numerical solutions could not conserved due to an error diffusion [4]. Moreover, the 2-D description in the overall region of tokamak is quite complicated since it is necessary to perform calculations on

both open and closed field lines simultaneously. Therefore, the particular conditions encountered in a mesh require very special treatments to simulate the 2-D model with conserving physical aspects.

### **2.1.1 Field alignment**

In a magnetized plasma, charged particles that are tied to the magnetic field, which leads plasma motions in along the magnetic field are fast streaming motion but those of radial direction to the magnetic field are a diffusion characteristic due to a random walk process. These different time and spatial scale of transport processes are need to be solved separately and that requires every cell of a mesh must be located on the flux surfaces in the FVM discretization. If a cell from such a grid were to be naively divided without taking into account the underlying magnetic field structure, this would likely cause spurious diffusion. If a mesh is not aligned with flux surfaces, therefore, numerical simulations not guarantee plasma in fusion experiments due to the possibility that mismatch between parallel and perpendicular flow of transport. For example, the electron thermal conductivity in the direction parallel to the magnetic field can exceed that in the perpendicular direction by several orders of magnitudes. In the absence of alignment, heat convection in the parallel direction would spuriously add to radial diffusion to the normal flux surfaces, thus causing unacceptable errors [4]. As a results, it is mandatory to align the mesh with magnetic flux surfaces when modelling transport in a highly magnetized plasma. To be

specific, in an aligned mesh made of quadrilateral cells every cell must have two sides parallel to the local flux surface.

### 2.1.2 Orthogonality

In addition to field alignment, it is also convenient that every cell is satisfied with a local orthogonality. This has the advantage for allowing a three-cell discretization of the parallel and perpendicular flows. It also has some desirable numerical properties, such as conservation and positive definiteness [10]. In addition, the orthogonal mesh is more proper for adapting orthogonal coordinates which are widely used to solve fluid plasma modeling. It helps saving time by skipping unnecessary calculations.

In equation (2.1), each convective term of the plasma transport equations, which includes the parallel flow, perpendicular drift and radial diffusion, respectively, can be expressed as [2]

$$\int dV \nabla \cdot (\hat{b} n u \phi) = (n u \phi)_e (b_e \cdot \bar{A}_e) + (n u \phi)_w (b_w \cdot \bar{A}_w) \quad (2.2)$$

$$\int dV \nabla \cdot (\hat{b} n u_r \phi) = (n u_r \phi)_e (b_e \cdot \bar{A}_e) + (n u_r \phi)_w (b_w \cdot \bar{A}_w) \quad (2.3)$$

$$\int dV \nabla \cdot (\hat{r} n u_r \phi) = (n u_r \phi)_n |A_n| - (n u_r \phi)_s |A_s| \quad (2.4)$$

with

$$\hat{b}_{e,w} \cdot \overrightarrow{A_{e,w}} = \left(\frac{B_p}{B}\right)_{e,w} (\hat{t} \cdot \vec{A})_{e,w} \quad (2.5)$$

$$\hat{w}_{e,w} \cdot \overrightarrow{A_{e,w}} = \left(\frac{B_t}{B}\right)_{e,w} (\hat{t} \cdot \vec{A})_{e,w} \quad (2.6)$$

Here,  $\phi$  represents one of the dependent variables and  $\vec{A}_i$  ( $i = e, w, n, s$ ) denotes the area vector at the cell face as illustrated in Figure 2.2.

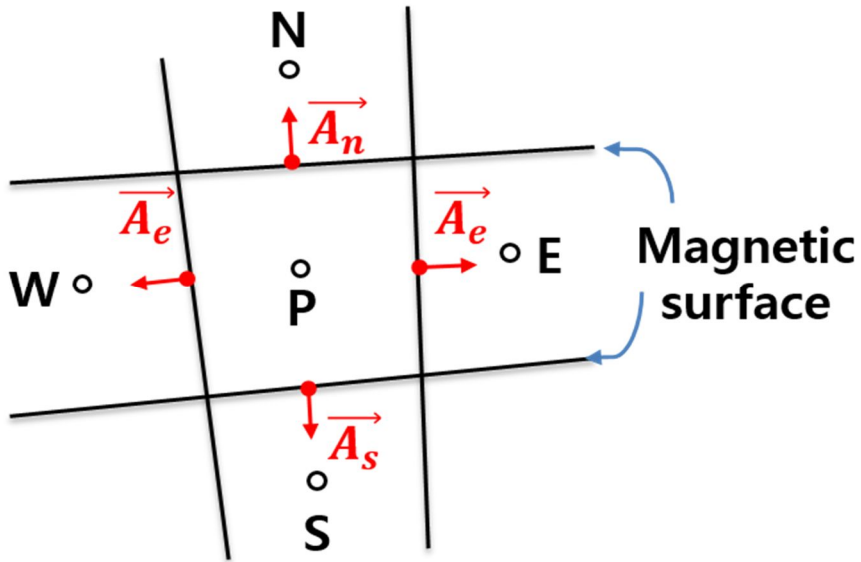


Figure 2.2 Control volume used in the FVM discretization. Calculation points are assigned at the geometric centers (P, E, W, N, S) of the control volumes (computational cell), and the mid-points (e, w, n, s) of the faces of a given cell.

The unit vector  $\hat{t}$  is tangential to the local magnetic surface in the poloidal plane. Equation (2.4) does not include magnetic pitch angle and vector  $\hat{t}$  by assuming that the northern and southern sides are normal to the magnetic surfaces [2], i.e.,

$$\hat{b} \cdot \overrightarrow{A}_{n,s} = 0 \quad (2.7)$$

If equation (2.7) is not obeyed at any cells in calculation domain, conservation law is broken locally and that small error would be a source for dispersion of numerical instabilities.

### 2.1.3 Adaptivity

In general, a static mesh cannot properly resolve travelling time dependent phenomena because equilibrium or plasma parameters change within transport time scale. Phenomena on the Alfvén time scale are much faster than relaxation processes such as the diffusion of the magnetic field and other transport phenomena [2]. This implies that a mesh must be reconstructed to represent equilibrium evolving per several iterations.

Accurate updating for a pedestal width at each time is important as well especially when other edge modeling codes are combined with transport solver to analyze edge plasma such as edge turbulence or ELMs models because that codes must be conducted only in the pedestal region [11]. Therefore setting of core-edge boundary separately is essential in practical usage of codes.

Moreover, the mesh is also needed to consider dynamic grid refinement and

coarsening to simulate transport phenomena more efficiently with time saving. For example, phenomena like moving detachment zone and core temperature profile whose gradient is very sharp near edge regions in the H-mode operation can only be modelled accurately when using dynamic grids [7]. This dynamic grid means mesh is generated automatically after several transport iterations but not passively by user selecting. Therefore, adaptive grid is the one of the important concept when mesh would be changed with time.

## **2.2 Specification of mesh development**

There are two types of meshes used in a two dimensional tokamak plasma modeling; the structured and the unstructured mesh.

The structured meshes consist of families of mesh lines with the property that members of a single family do not cross each other and cross each member of the other families only once, while the unstructured mesh does not have such a restriction. The advantage of the structured mesh is that any mesh node is uniquely identified by a set of two (2-D mesh) or three indices (3-D mesh) and thus is to access. In the unstructured meshes, a connection table is required to identify the relationship of the mesh nodes. Usually, the structured mesh is used for the Finite Difference Method (FDM) and the Finite Volume Method (FVM), while the Finite Element Method (FEM) often uses the unstructured mesh. In this work, a mesh is targeted for

structured mesh which is more preferable for FVM method.

The methods applied in the structured mesh generation are grouped into two categories; the algebraic method and the numerical method. The numerical method solve a set of Partial Differential Equations (PDEs) to determine the mesh distribution while the algebraic method generate mesh directly by interpolation. The numerical method are global approaches and can provide meshes with smooth transitions and orthogonality maintained but transform equation between physical space and logical space must be required to generate numerical mesh. Because there are no exact transform equations in a typical plasma configurations, our mesh generator adapts algebraic mesh generation. The algebraic method has also more suitable for adaptive grid concepts due to the fact that the algebraic method can always resolve a mesh with the minimum computational effort [12].

As a results, we adopt the structured mesh with the algebraic grid generation method and the developed mesh follows some constraints to consider critical mesh requirements for the tokamak plasma. The following describe in detail the numerical approaches used in this work.

- The developed mesh is intended for Finite Volume Method (FVM) discretization to separate anisotropy of transport characteristics in a tokamak plasma.
- The mesh has field-aligned curvilinear orthogonal grid. This infers

every grid points must be aligned the local flux surfaces and each cell is as rectangular as possible to follow locally quasi-orthogonal cell.

- The non-uniform grid distribution focused on a simulation purpose is possible to simulate more applicably to various plasma phenomena with saving time. This concept helps to make adaptive grid for preparation.
- Several non-uniform grid generation method in the core region are possible to generate automatic grid generation following various simulation conditions; arbitrary, stationary, subdomain mode.
- Two types of magnetic configurations is selected which is mostly used in tokamak operations; single null, connected double null.

### 2.2.1 Magnetic coordinate

To allow efficient treatment of the anisotropy caused by the strong magnetic field, it is useful to introduce local orthogonal coordinate system which has three basis vectors  $(\hat{b}, \hat{\psi}, \hat{w})$  satisfying the orthogonal relation [2],

$$\hat{w} = \hat{b} \times \hat{\psi} \quad (2.8)$$

where  $\hat{b}$  represents the unit vector along the magnetic field line (parallel direction),  $\hat{\psi}$  normal to the magnetic flux surface (radial direction), and  $\hat{w}$

normal to both  $\hat{b}$  and  $\hat{\psi}$  (perpendicular or diamagnetic direction). These magnetic coordinate are employed to describe the Braginskii's equation. In general this physical domain can be converted into the 2-D computational domain which has two coordinates  $(\hat{\chi}, \hat{\psi})$  by toroidal axisymmetric assumptions.  $\hat{\chi}$  is the direction of projection to the poloidal field in the toroidal plane and  $\hat{\psi}$  is perpendicular direction to the magnetic flux surface. Schematic figure is below in Figure 2.3. A realistic curvilinear geometry is treated and can be discretized with a structured flux-surface-fitted mesh generator.

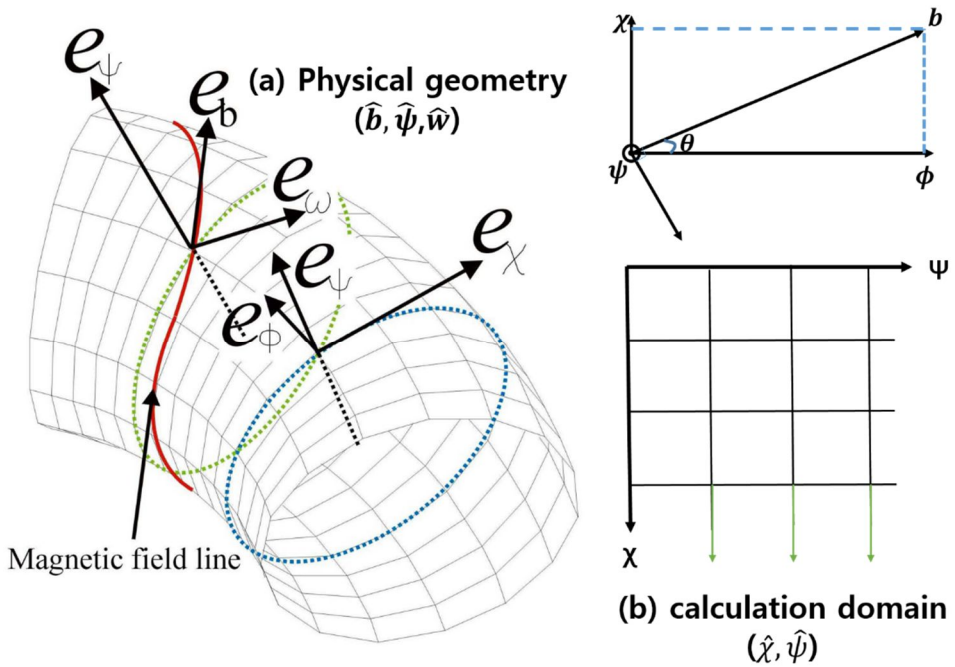


Figure 2.3 Magnetic coordinate system for the FVM discretization which has the two sets of orthogonal coordinate system. (a) physical domain and (b) calculation domain. (b) surface projected onto the poloidal cross section.

## 2.2.2 Magnetic field configurations

	Single Null	Double Null
<b>Separatrix number</b>	3	-6
<b>Region Number</b>	3	5
<b>Divertor number</b>	2	4

Table 2.1 Classification of possible magnetic configurations for diverted plasmas and conventions

To be specific, the magnetic configurations which can be readily treated are (a) Single Null (SN) and (b) Connected Double Null (or simply Double Null, DN) geometry. The code is not intended to generate magnetic geometries which have more than two X-points and limiter configuration. The single null geometry is well known for being the most commonly used in today's experiments. This is indeed the configuration considered for ITER [13]. It is also used on ASDEX Upgrade, JET, DIII-D, and JT-60U, and a number of other machines. The double null geometry, while now less fashionable, has been investigated on several machines such as KSTAR [14]. In this geometry there are two X points and two associated pairs of divertor plates. This code is not aim to create disconnected double null where two X-points not to lie on exactly the same flux surfaces.

In the construction of a mesh, some ordering is required for the X-points. Separatrices will be fragmented into segments, and regions will be defined

within the simulation domain. Also, every divertor plate needs to be identified as a distinct structure in the code and ordered according to the separatrix number.

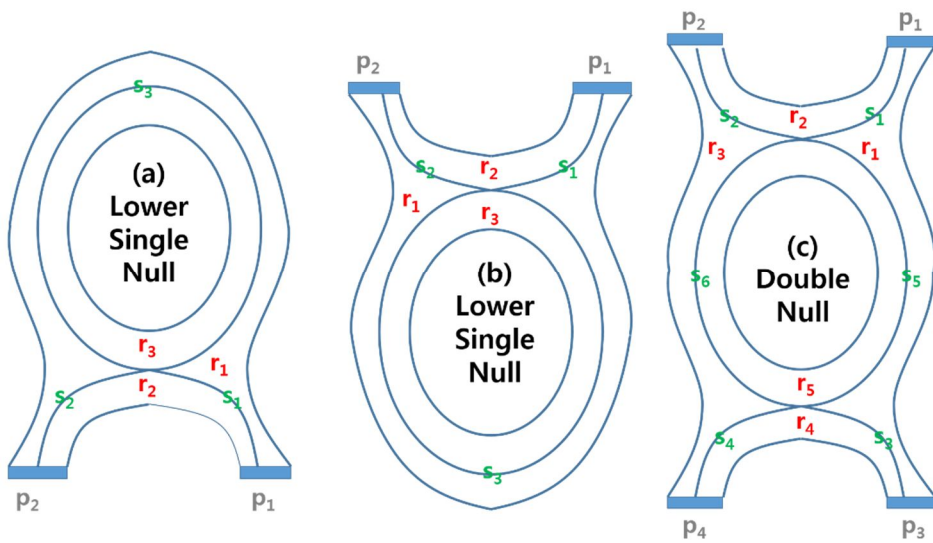


Figure 2.4 Schematic representation of the (a) upper single null geometry, (b) lower single geometry and (c) double null geometry. Indices of separatrix segment, divertor plates and regions are indicated by numbers prefixed with s, p and r, respectively.

## **Chapter 3**

# **Vector Following Orthogonal Mesh Generation**

### **3.1 Methodology for orthogonal mesh generation**

#### **3.1.1 Vector following method**

A direction vector is demanded for tracing any desired point to search boundary layer and orthogonal position as well because the algebraic method generates a mesh directly using an interpolation scheme. In this code, the grid points composing quadrilateral orthogonal meshes are determined by following a direction vector obtained from the poloidal magnetic fields [15]. This method has advantages of making mesh more efficiently with accuracy and considering plasma conditions at the arbitrary regions. In addition, the size of direction vectors is adjusted arbitrarily by user, which results in low sensitivity to grid resolution than other grid based interpolation methods.

##### **a) 2-D poloidal magnetic field map**

The relation between the equilibrium poloidal magnetic flux surface and the poloidal magnetic field is represented as below.

$$\vec{B}_{pol} = \frac{1}{2\pi} \nabla \varphi \times \nabla \psi \quad (3.1)$$

Equation (3.1) implies poloidal magnetic flux surfaces are simply calculated from contours lines of the function  $\psi$  and each poloidal magnetic fields lies on the equal poloidal magnetic surfaces. This means equal  $\psi$  surface is determined simply by just following  $\vec{B}_{pol}$  and gradient of  $\psi$  is the direction of the normal to  $\vec{B}_{pol}$ . The expression of poloidal magnetic field is related to the derivative of  $\psi$  with respect to the R and Z.

$$B_R = -\frac{1}{R} \frac{\partial \psi}{\partial Z}, \quad B_Z = \frac{1}{R} \frac{\partial \psi}{\partial R} \quad (3.2)$$

### b) Derivative

It is essential for calculating of derivative of  $\psi$  to know poloidal magnetic fields at each grid. For reducing discrete error at least, higher order central differential scheme is adapted and the derivative of  $\psi$  in the x-direction (R,Z) is solved as order of four error of a grid size.

$$\left( \frac{\partial \psi}{\partial x} \right)_i = \frac{-\psi_{i+2} + 8\psi_{i+1} - 8\psi_{i-1} + \psi_{i-2}}{12\Delta x} + O(\Delta x)^4 \quad (3.3)$$

Here  $O(\Delta x^4)$  is the Taylor discrete error. Using equation (3.2) and (3.3), poloidal magnetic fields at every points are determined.

These point values at each grids are used for interpolation to knowing two dimensional poloidal field map. Bilinear interpolation is a simple way to approximate the value at unknown point by using four corner value of each cells. After setting of interpolating function of two variables (x and y) on a regular two dimensional grid, four coefficients are founded out through four known points.

$$a_{00} = [x_2 y_2 f(Q_{11}) - x_1 y_2 f(Q_{21}) - x_2 y_1 f(Q_{12}) + x_1 y_1 f(Q_{22})] / (\Delta x \Delta y) \quad (3.4)$$

$$a_{10} = [\{f(Q_{21}) - f(Q_{11})\} y_2 + \{f(Q_{12}) - f(Q_{22})\} y_1] / (\Delta x \Delta y) \quad (3.5)$$

$$a_{01} = [\{f(Q_{21}) - f(Q_{22})\} x_1 + \{f(Q_{12}) - f(Q_{11})\} x_2] / (\Delta x \Delta y) \quad (3.6)$$

$$a_{11} = [f(Q_{11}) - f(Q_{21}) - f(Q_{12}) + f(Q_{22})] / (\Delta x \Delta y) \quad (3.7)$$

$$\Delta x = x_{i+1} - x_i, \quad \Delta y = y_{i+1} - y_i \quad (3.8)$$

The values of  $f(\vec{B}_{pol}$  or  $\psi$ ) at arbitrary points are expected as below.

$$f(x, y) = a_{00} + a_{10}x + a_{01}y + a_{11}xy \quad (3.9)$$

### c) The sequence of vector following method

In a given poloidal magnetic field map, direction vector is calculated by using the Runge-Kutta method which has 4<sup>th</sup> order accuracy of a grid size. This vector following method is capable for finding any points depending on the indication of direction vector while a step size of direction vectors is adjusted arbitrarily. Once tracing an expected position of desired  $\psi$ , the actual position of  $\psi$  is determined by the linear interpolation. This sequence

is repeated until grid point meets constraint points (divertor structure) or initial points when direction vector is for circulation of equal  $\psi$ . The general vector following sequence is in Figure 3.1.

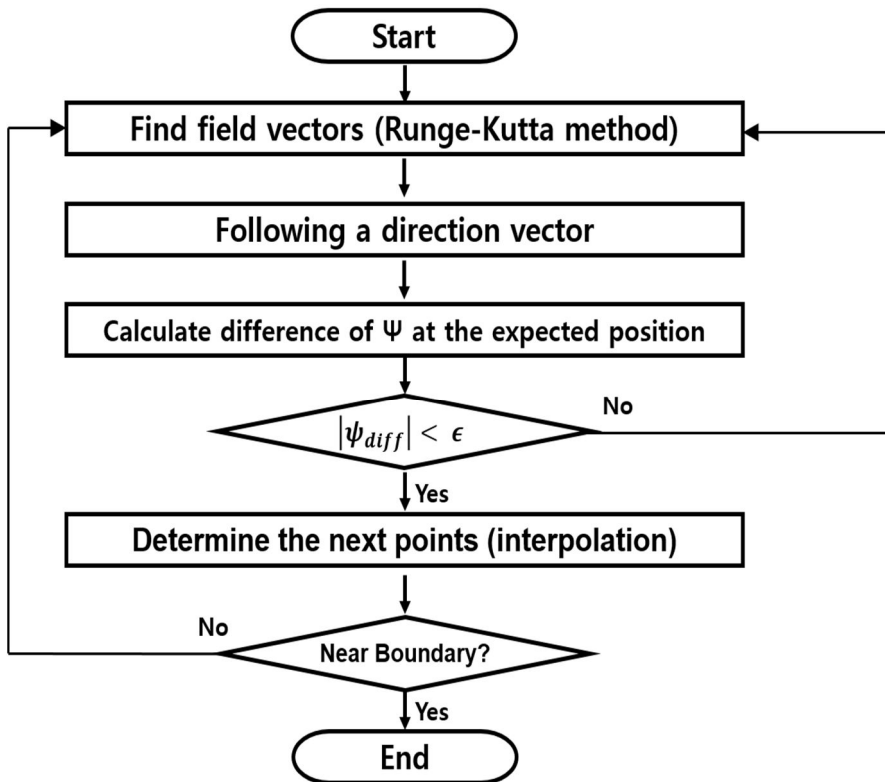


Figure 3.1 Flow chart of the vector following method

### 3.1.2 Definition of the magnetic field configurations

Prior to a mesh generation, a plasma boundary must be defined to know plasma configurations and set initial grid distribution. While conventional mesh generator for magnetic null data is offered from input data or passively selected by user [4], it is mandatory to determine magnetic geometry for the automatic mesh generation which is preferable when considering adaptive grid concept. In a bid to maintain flexibility of grid, plasma magnetic configurations are determined automatically by some investigations and divided into three mesh types; lower single null, upper single null and double null. These configurations are simply determined by finding both the number and the null position of poloidal magnetic field.

#### a) Determination of separatrix lines

The magnetic null point where  $\psi$  is a local extremum to minimum (or maximum) is created by sum of plasma current and auxiliary coil current. At both magnetic axis (or O-point) and near separatrix (X-point), the  $\nabla\psi$  has nearly zero but the functional shapes at these points appear different characteristics due to the difference of second derivate of  $\psi$ , which allows separating two points numerically whether a test point is critical point or saddle point through discriminant.

Equation for the magnetic field null is expressed briefly.

$$\nabla_R \Psi(R, Z) + \nabla_Z \Psi(R, Z) = 0 \quad (3.10)$$

After calculating the bilinear interpolation coefficient of equation from (3.4) to (3.7), field null points can be determined by solving quadratic equations of interpolation functions.

$$a_x + b_x x + c_x y + d_x xy = \frac{\Psi(x, y)}{dx} = 0 \quad (3.11)$$

$$a_y + b_y x + c_y y + d_y xy = \frac{\Psi(x, y)}{dy} = 0 \quad (3.12)$$

Combine equation (3.11) and equation (3.12)

$$(d_x c_y - c_x d_y) y^2 + (d_x a_y - c_x b_y + b_x c_y - a_x d_y) y + (b_x a_y - a_x b_y) = 0 \quad (3.13)$$

Equation (3.13) has two roots and the real values located inside testing cell will be null points, X-point or magnetic axis

Each null points of interest must be tested against its nearest neighbors to locate the regions where  $|\nabla\psi|^2$  is a local minimum. At these points, let the equation [16]

$$D(R, Z) = \left(\frac{\partial^2 \psi}{\partial R^2}\right) \left(\frac{\partial^2 \psi}{\partial Z^2}\right) - \left(\frac{\partial^2 \psi}{\partial R \partial Z}\right)^2 \quad (3.14)$$

If  $D > 0$  at a critical point, then the critical point is a local extremum regarded for a magnetic axis and the sign of  $\left(\frac{\partial^2 \psi}{\partial R^2}\right)$  and  $\left(\frac{\partial^2 \psi}{\partial Z^2}\right)$  make it clear whether the point

is a maximum of a minimum. On the contrary, If  $D < 0$  at a critical point then the critical point is a saddle point and there is an X-point where separatrix line is nearby. The number of X-points is used to determine magnetic configuration as single null or double null configuration and this information proposes initial vector positions to find separatrix line and set a reference boundary of mesh regions.

#### **b) Field configuration and ordering**

After finding field null points, a plasma boundary is identified by following a contour curve of equal  $\psi$  at the X-point and then other boundaries (SOL, private, core region) also discovered by divertor constraint and core-edge penetration value. Some ordering is conducted in this process such as segments of separatrix, divertor plates and the regions of the simulation domain [4]. The ordering method is followed in Figure 2.4 as previous chapter. Figure 3.2 shows the initial magnetic configuration and boundary with poloidal field vector. The direction of poloidal field is counter-clockwise or clockwise which is caused by toroidal plasma current. The difference of field direction makes difference of a starting point when mesh is created in the next step.

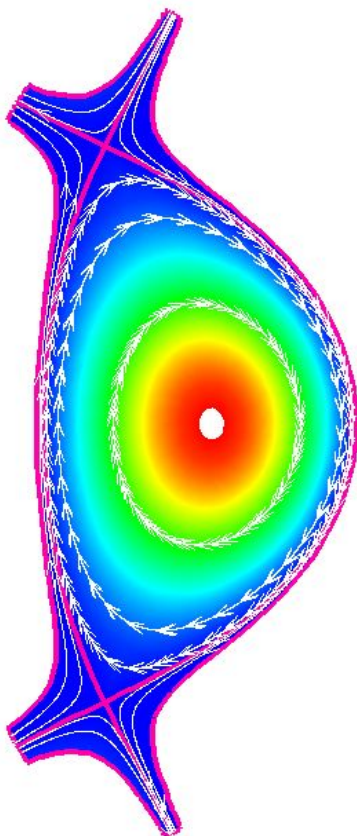


Figure 3.2 Schematic view of the magnetic field configuration and poloidal magnetic field direction in the double null configuration.

### 3.1.3 Non-uniform grid generations

In this numerical work, the arbitrary grid distribution is available for providing calculation domains more accurately with time saving. An initial grid distribution is set by user's interest using deviation parameters. After

that, core distribution will be changed by accepting plasma parameters such as temperature profile and 1-D core equilibrium profile for radial core distributions.

### a) Stretching function for initial distribution

The stretching function are used to distribute computational nodes along the plasma boundary (separatrix) and radial distributions with several parameters ( $E, D, S$ ) [17].

$$s_i = \sum_1^{i-1} \left[ \frac{2}{e^\phi + e^{-\phi}} \right]^E / \sum_1^{i-1} \left[ \frac{2}{e^\phi + e^{-\phi}} \right]^E \quad (3.15)$$

$$\phi = \left[ \frac{i-1}{N} - D \right] \times S \quad (3.16)$$

where  $s_j$  is relative location;  $i$  is the label of one point;  $N$  is the total number of points along the separatrix line;  $E$  ( $= -1,0,1$ ) is the deviation parameter;  $S(>0)$  is the parameter used to control the degree of stretching, called scale parameter.

With this stretching function, the location of any node in on line AB in Figure 3.3 is calculated by

$$x_i = x_A + (x_B - x_A) \cdot s_i \quad (3.17)$$

The exponential parameter ( $E$ ) determines the characteristic of the

distribution; contraction to a point, repulsion from a point, or uniformity. If  $E = -1$ , the distribution is contracting the point; if  $E = 1$ , the distribution is repulsing from the point; and if  $E = 0$ , the distribution is uniform. The deviation parameter ( $D$ ) provides the relative location of this point along AB. For example, if  $D = 0.5$ , this point is located at the center. The scale parameter  $S$  controls the degree of stretching. The larger  $S$  is, the more the distribution is stretched. If  $S = 0$ , the distribution is uniform.

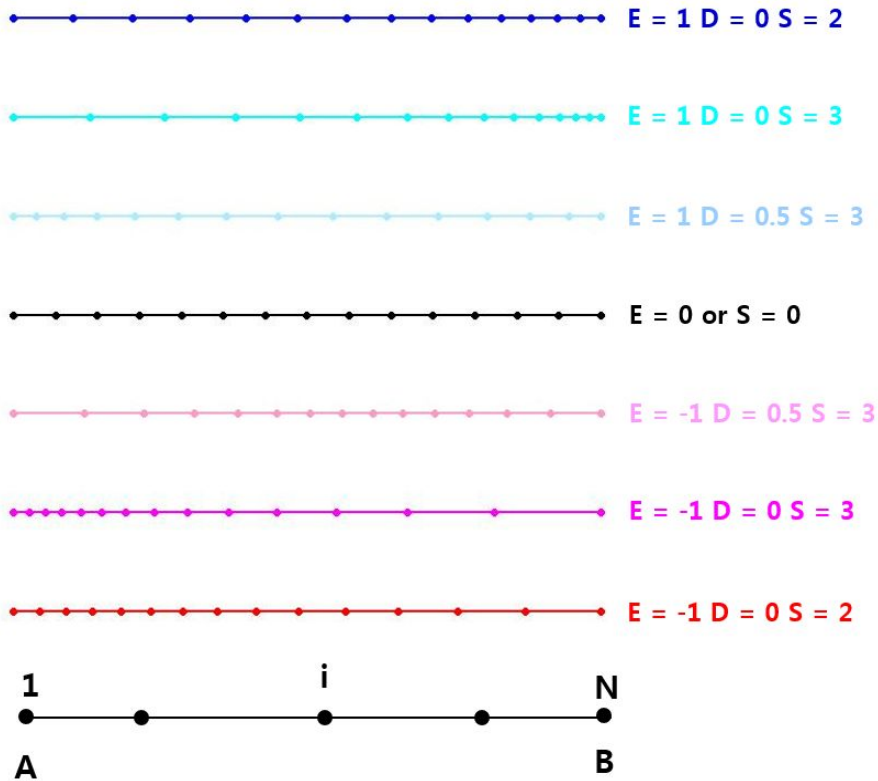


Figure 3.3 Nodal distribution on one line and effects of  $E, D$ , and  $S$

The distribution for a specific problem should be determined by user. For example, it is possible to make small node spacing at the near divertor plate to analyze divertor physics and node spacing on inner separatrix is narrower than outer one due to toroidal field effect which affect the scale of transport phenomena on the poloidal plane.

### **b) Adaptive core distribution**

Distribution in a core region will be changed by considering simulation conditions. If a plasma is stationary with smooth variations of profile, the temperature profile is accepted as a reference distribution parameter. When a subdomain for additional calculations is needed in the core region, distribution is allocated separately after setting a boundary of two domain in the core.

### **Stationary mode**

Because the spatial scale length in radial direction is generally in correlation with the local Lamor radius  $\rho_i \propto \sqrt{T_i}$  [18], which may vary substantially from the core to the edge of the plasma, it is useful to distribute a non-uniform grid with the grid size in the radial direction correlated with the local Lamor radius for improved spatial resolution and efficiency. Therefore flux surfaces will be distributed based on the ion temperature profile presented from the plasma transport solver, which results the radial distribution will be updated adaptively with transport time scale.

Grid size in real space (R, Z coordinate) to be correlated with the ion temperature as follow.

$$\Delta r \sim \frac{\Delta T_{ref}}{\nabla T}, \quad \Delta T_{ref} = \frac{\Delta T_{tot}}{N} \quad (3.18)$$

where  $T_{tot}$  is the difference of the ion temperature between a boundary of core center and a separatrix.  $\Delta r$  can be varied according with  $\nabla T$  that results more refined grid at a large gradient region and coarse grid at a small gradient region.

### **Subdomain mode**

For more sophisticated 2-D simulations, additional codes connected to the main transport solver is needed like as an edge turbulence code for providing anomalous transport coefficients at the edge regions [2]. These so-called, sub-modules are also essential to be installed for the integrated simulation of global scenario modeling including mode transition analysis. But some sub-codes is operated only a specific domain not fully calculated overall core region, domain decomposition in the core region is required in that cases. For a treating above situations, subdomain mode is helpful to separate more two region in the core region.

The 1-D equilibrium data which results from the equilibrium solver such as normalized effective minor radius ( $\rho_n$ ) and normalized flux surface ( $\psi_n$ ) can be used as a reference distribution parameters. For example, pedestal point and width is determined to analyze edge physics by finding  $\rho_n = 0.95$  and

$\psi_n$  at that point [11]. The real  $\psi$  can be deduced using the  $\psi_n$  as well. Therefore core and edge domain are defined individually and automatic radial distribution is possible for utilizing the edge turbulence code.

### 3.1.4 Normal vector tracing

As mentioned previously, computational domain should be generated quadrilateral elements as rectangular shape as possible, while remaining conform to the actual (in general non-orthogonal) boundaries. In this work, orthogonal mesh is created by following normal vector of poloidal magnetic field according to the nodal distribution along the contour curve of each flux surfaces. The following of normal vector is continuing by using the Runge-Kutta method as before until finding the next flux surface that has different level and an expected position in which the normal vector indicates turns into normal to the next flux surface by linear interpolation.

This vector tracing scheme does not ensure mathematically perfect orthogonality at each cell but this method is more proper when considering multiple mesh generation with updated equilibrium profiles while reducing the computational time. In addition, since we don't know the relation of the coordinate transformation (or inverse transform) from the physical space to the logical space, the numerical mesh generation is impossible in that cases.

However, this method is not consistent in entire regions where the distribution point is near a boundary such as the divertor plate or the separatrix line closed to the X-point, which leads to a mesh tangled problem

that results in an error in calculations of the transport equation. To resolve these problems, two constraints are added to a particular area.

1. If a grid point are too close to a divertor plate (lower than  $\epsilon$ ), there is a bias to force direction of vector be similar to the direction of divertor plate.
2. There is also a bias to prevent two neighbouring points from getting poloidally too close. This constraint commonly used nearby X-point where radius of the curvature is large.

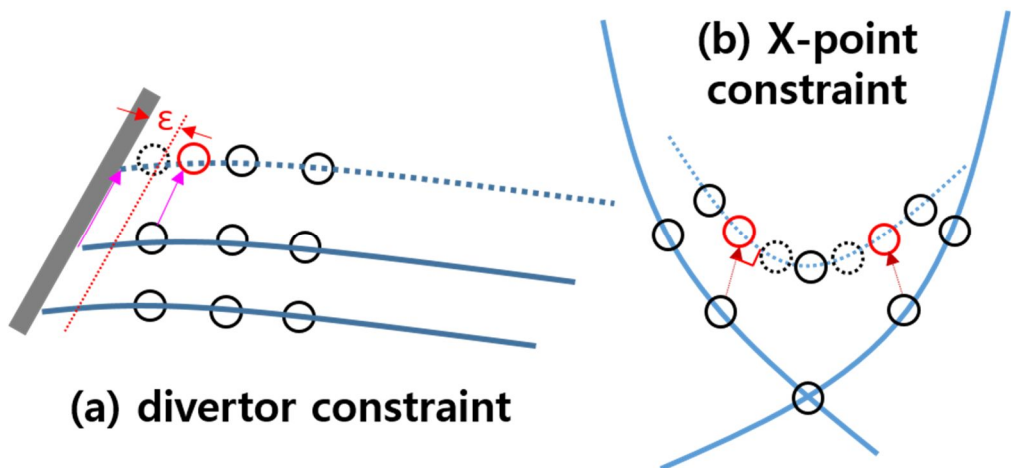


Figure 3.4 Two constraints during the normal vector tracing. (a) divertor constraint and (b) X-point constraint

## 3.2 Numerical procedure

Using the above methods, orthogonal meshes will be generated in the procedure shown below [4].

### 1. Identification of the magnetic field configuration

After reading the poloidal flux function  $\psi$  on a rectangular (R,Z) array, the derivatives of  $\psi$  with respect to R and Z are calculated to get the poloidal magnetic field map, and all the points where  $\nabla\psi$  vanishes are identified by grid scan and interpolation scheme. There should be at least two such points which are classified into two branch by discriminant; one for and X-point and the other for the magnetic axis point. By calculating number of X-point and its positions, mesh configuration is defined here for single null or double null geometry.

### 2. Determination of the plasma boundary

Once the X-points are known, all segments of separatrix need to be parametrised. This is done by calculating the contour curves which pass through these X-points by following direction of poloidal magnetic field. The separatrices are calculated starting from their respective X-point and they are constructed so as to stop at the point of intersection with a divertor plate. Divertor plates are in fact defined during this process. The segments of separatrix and divertor plate are then numbered as described in Figure 2.4. The next step is then to find the outer boundaries in the SOL and private

regions. This is accomplished by stepping along the divertor plates, on either side of the point of intersection with a separatrix. At each step the flux surface intersecting the plate is continued to reach the boundary value of  $\psi$  in SOL or private regions.

There remains to determine a boundary the SOL and the core region. This is done by selecting depth of that boundary (flux surface) as measured from the X-point towards the magnetic axis. Given the separatrices and boundaries, the various regions are readily constructed.

### 3. Distribution of grid points on the initial flux surfaces

The first step is to define an initial distribution of grid points poloidally. At this stage the stretching function is used to make various segments of separatrices and arbitrary distribution of points can be specified on every segment separately as equation (3.15). This procedure is applied on every segments of separatrix individually.

Flux surfaces can be distributed arbitrarily within any individual region. In the code a non-uniform radial distribution is made by stretching function initially but core distribution could be changed as various simulation conditions. If a plasma is slowly varying with time with fast relaxation process without any sub-codes, ion temperature is selected as reference distribution parameter. If an additional codes is connected into transport code for modeling of specific plasmas conditions, the subdomain mode is recommended to set boundary and distribute separately in a core domain.

#### 4. Orthogonal mesh generation from a flux surface to the next

Now that a distribution of points is given on one boundary in every region, one can proceed with the mapping of these points onto neighboring flux surfaces, all the way to the opposite boundary. The normal vector tracing scheme is used in this stage to finding the normal points on a next flux surface. Starting at the separatrix lines, the normal vector traces the orthogonal positions to the distributed psi value and rectangular cell is constructing by considering neighbor points while keeping the actual flux surface where two constraints effect the non-orthogonal shape near boundary regions. This sequences are continued until normal vectors meet  $\psi$  boundary at each regions.

## Chapter 4

### Verification of the Developed Code

In a time varying equilibrium case of the core region, initial grids in the SOL and private region are generated once when the simulation starts. These regions are assumed to be fixed during the rest of the simulation. But the computational grids inside the separatrix must be reconstructed in the course of simulation using the  $\psi(R,Z)$  at the current time step from the MHD equilibrium solver with the prescribed separatrix positions. The vector following mesh generator is target for automatic grid distribution in the core region, therefore, two dimensional  $\psi$  map is required for initial distribution before transport simulation and then plasma parameters such as ion temperature and 1-D equilibrium profile are needed for next grid generations in the core region.

In this thesis, initial equilibrium data is acquired from the free boundary MHD equilibrium code named Tokamak Equilibrium Solver (TES) [19] for grid generation test. This code calculates the 2-D distribution of the poloidal magnetic flux,  $\psi(R,Z)$  obtained by solving the Grad-Shafranov equation. The target equilibrium configuration is KSTAR which is enable to have various magnetic shapes including LSN, USN, and DN geometry. The

divertor structure data is also offered in advance due to constrain and determine boundary of separatrix line and SOL region.

## **4.1 Initial conditions for the reference mesh generation**

### **4.1.1 Grid refinement of non-uniform grid distribution**

In an initial grid distribution, stretching function in equation (3.15) can be used for non-uniform grid spacing and grid refinement and coarsing are not entirely arbitrarily. Normally, gradient of plasma variables usually get larger near boundary regions such as divertor plate, separatrix and X-point, so initial distribution is followed by refinement at the boundary layer.

The distribution is divided into two ways; the poloidal and the radial direction. Once grid points have been distributed poloidally on a given flux surface, the distribution of points on nearby flux surfaces is largely determined. Thus the initial poloidal distribution is important for the suitable calculation domain because grid points are fixed poloidally over the entire simulations. In general, divertor separatrix line can be distributed refinement near the divertor plate where ion temperature is highly changed poloidally for accurate heat flux calculation. But in a detachment plasma, a movement of low temperature region is appear so non-uniform distribution is need to be reallocated along the separatrix lines in that case.

For the balance geometric configuration, core separatrix distribution is recommended to be uniform but that would be changed when poloidal asymmetric cases. Core distribution is assigned to be uniform since the transport code accepts an initial grid with a same interval [2]. But this uniform distribution could be changed after several iterations as the equilibrium evolves.

Region	1	2	3	4	5
Domain	Outer SOL	Upper private	Inner SOL	Lower Private	Core
$E(\chi, \psi)$	1, -1	1, -1	1, -1	0, -1	0, 0
$D(\chi, \psi)$	0, 0	0, 0	0, 0	0, 0	0, 0
$S(\chi, \psi)$	3, 2	3, 2	3, 2	3, 2	0, 0

Table 4.1 Reference grid distribution parameter of the stretching function at each regions for the KSTAR double null configuration.

#### 4.1.2 Initial distribution shapes of diverted plasmas

Figure 4.1 shows the contour plot of the two dimensional initial equilibrium profile for the reference mesh generation. The developed mesh generator reads the equilibrium data 2-D  $\psi(R,Z)$  and also 1-D equilibrium profile like

$\rho_n, \psi_n$  as well. The divertor structure positions is determined prior to the determining the separatrix lines by reading geometric data.

The reference mesh can be generated assigning the initial grid node numbers both poloidally ( $\chi$ ) and radially ( $\psi$ ) as below Table 4.2. As a results, the reference constructed mesh is in Figure 4.2 (a). In addition, other equilibrium cases are also tested for the lower single null and upper single dull geometry to verify the mesh generation for the various configurations in Figure 4.2 (b) and Figure 4.2 (c)

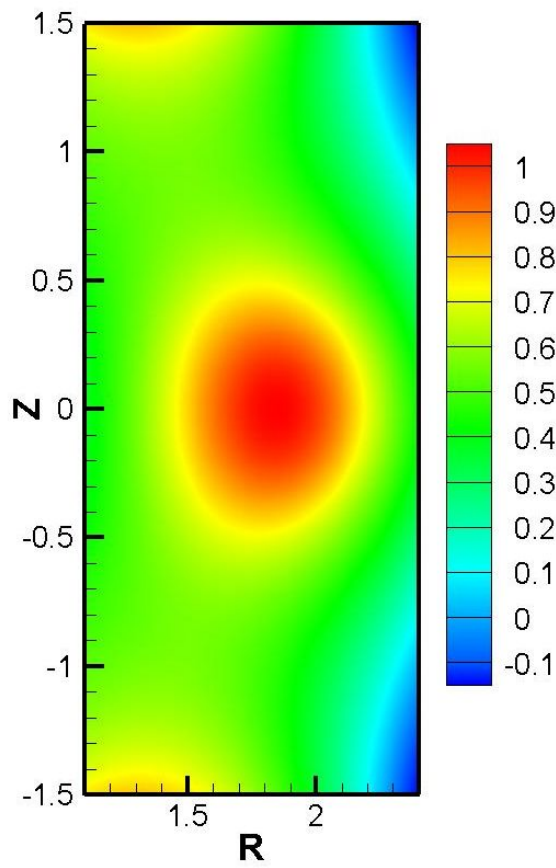


Figure 4.1 Initial equilibrium from the TES code of the KSTAR double null configuration.

Region	1	2	3	4	5
Domain	Outer SOL	Upper private	Inner SOL	Lower Private	Core
Node number ( $\chi, \psi$ )	79 x 10	29 x 10	59 x 10	29 x 10	81 x 20

Table 4.2 Initial grid node numbers of KSTAR double null configurations for the reference mesh generation.

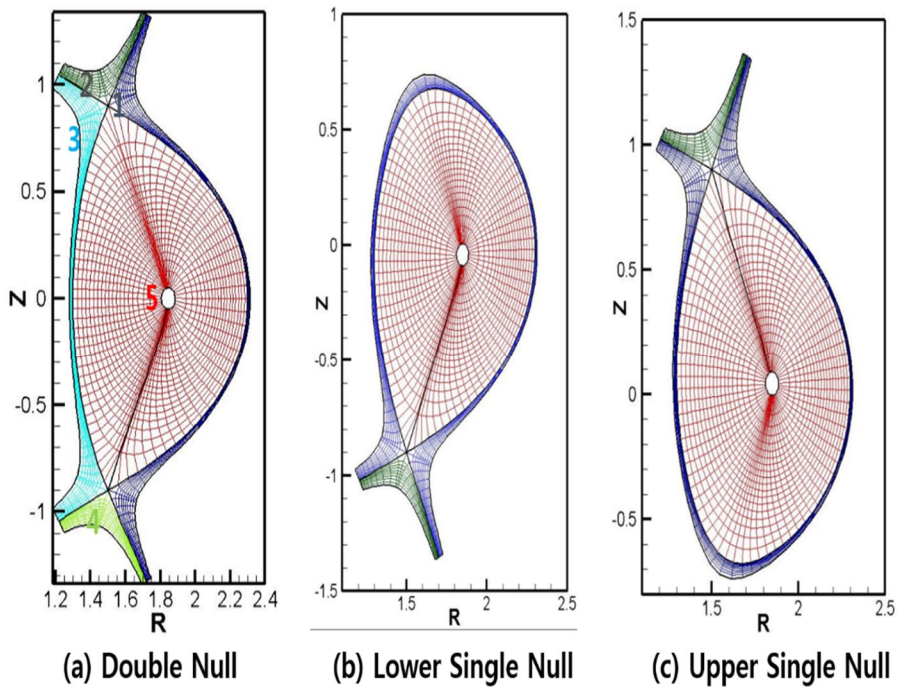


Figure 4.2 The result of the constructed mesh of the various KSTAR configurations. (a) reference Double Null (DN) and (b) Lower Single Null (LSN) and (c) Upper Single Null (USN) configurations.

## 4.2 Evaluation of the mesh quality

For an evaluation of a created mesh, several mesh quality factors are adapted based on a criterion for using FVM method as mentioned in chapter 2.1.1 and 2.1.2. The FVM form equations have to follow flux conservation theorem but each cells in calculation domain is slightly deviate that. So if a deviation from an ideal mesh shape is high, simulation results in a real mesh do not guarantee the numerical accuracy and stability. Figure 4.3 shows the schematic diagram of a control volume for discretization in FVM and deviation.

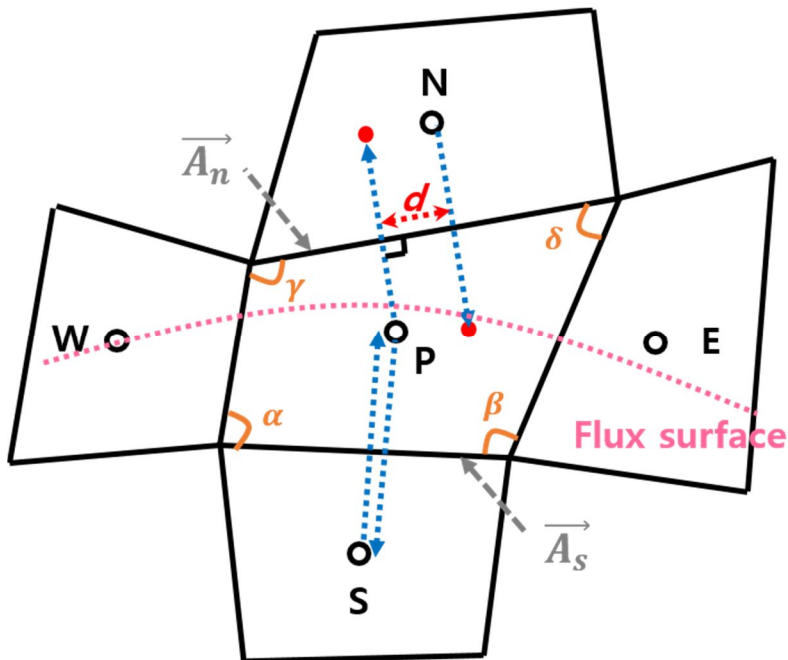


Figure 4.3 Schematic diagram of a control volume for discretization in FVM and deviation.

## 4.2.1 Quality factor

### a) Standard deviation of average flux surface

This factor is related to the concept of field alignment as followed in chapter 2.1.1. To test whether grid points are located to the equal flux surface, a flux surface ( $\psi$ ) in each cell centers is scanned poloidally at each radial flux label by following  $\psi$  contour curve. After a poloidal scanning, an average value of the  $\psi$  is calculated and standard deviation of  $\psi$  from the average is also obtained. The dashed line of flux surface in Figure 4.3 shows the brief schematic view of field misalignment concept.

### b) Cell orthogonality

Local quasi-orthogonality secures geometrical quality of mesh which is closely related to the rectangular shape. Thus, degree of deviation from a rectangular shape is obtained as below equations.

$$\sigma_{orthogonality} = \sqrt{(90 - \alpha)^2 + (90 - \beta)^2 + (90 - \gamma)^2 + (90 - \delta)^2} \quad (4.1)$$

This standard deviation of cell orthogonality can be a standard for orthogonal shape of each cell. In general, algebraic mesh is not ensured mesh smoothness and uniformity, which implies that if equation (4.1) is high of peaked at some points, numerical stability is possible to be broken at that regions.

### c) Radial flux deviation

As mentioned in the previous equation (2.7), all radial flux at an each cell are assumed to be normal to the local flux surface. If equation (2.7) is not satisfied at any cells, radial conservation is broken locally. Figure 4.3 indicates the example of possibility radial flux deviations if bottom and top surfaces of cell are not parallel to the flux surfaces. To minimize this deviation value, radial flux vector at every cells must be reach to the next cell center. So breaking of equation (2.7)'s assumptions is a measure for a deviation of radial flux deviation and this concept is calculated as follow.

$$\text{Radial flux deviation} = d / \left| \vec{A}_n \right| \quad (4.2)$$

$d$  is a distance between two flux on a crossing flux surface and  $|\vec{A}|$  an area of cell surface.

#### 4.2.2 Measurement of mesh quality for the reference distribution

The mesh quality factors are measured for the double null configuration as shown in Figure 4.2 (a). To analyze general characteristics of the property, the contour plot of deviation parameters is sketched in Figure 4.4. The  $\psi$  deviation is also calculated and plotted radially in Figure 4.5.

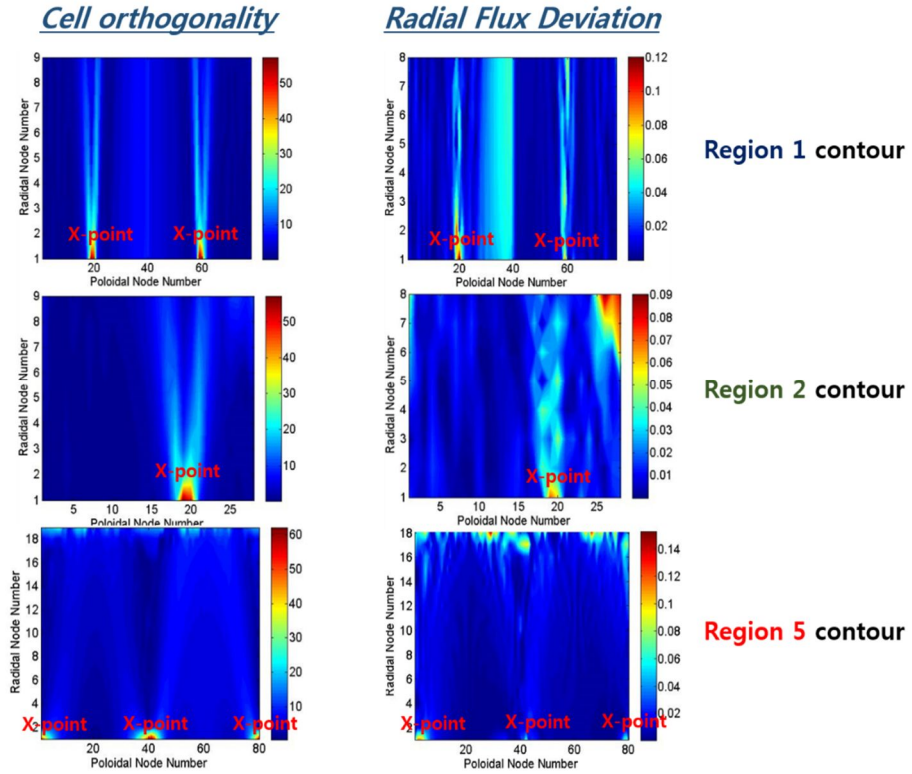


Figure 4.4 Contour plots of the average quantities of (a) cell orthogonality and (b) radial flux deviation at each regions for the reference double null configuration.

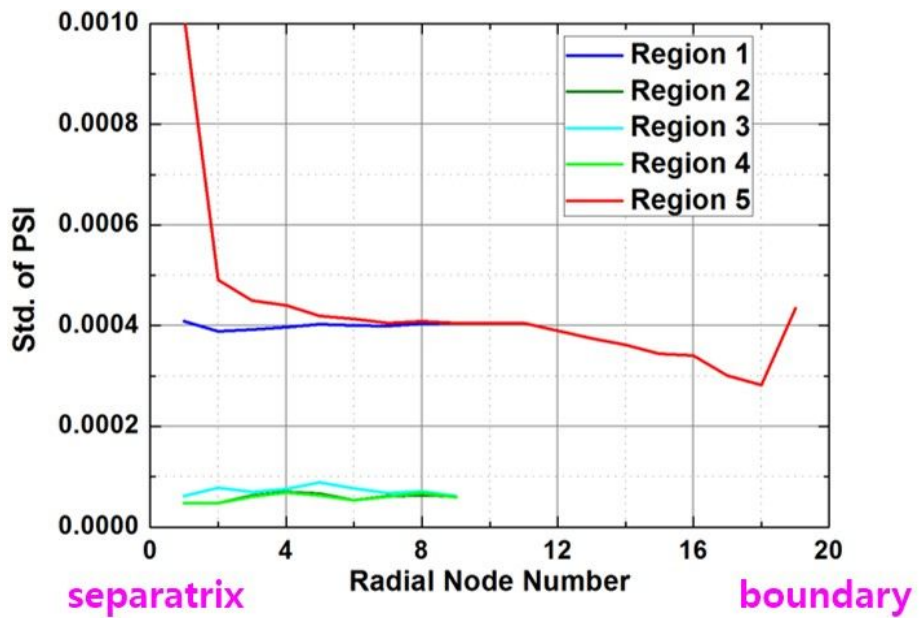


Figure 4.5 Radial variations of standard deviation of  $\psi$  at each regions for the reference double null configuration.

Clearly, Figure 4.4 shows the most deviations occur at the vicinity of boundary layer. Especially, the peaks of cell orthogonality and radial flux deviation are appear near X-point and errors disperse radially because a constructed mesh shape is not guaranteed perfect orthogonal shape due to the X-point constraint that prevents entangled mesh. Therefore drastic radial curvature variation near the X-point is the main reason for breaking of orthogonality.

In comparison with other regions, the core region is the most highly deviated area for all deviation parameters as indicated both in Figure 4.4 and Figure 4.5. This results came from wide grid spacing owing to large calculation domain. As referred in Figure 4.2, core region is the most largely broad area than any other region and cell area is also the biggest. In particular, intervals of grid spacing near the separatrix and the core center are distinctively large.

For reducing the deviation values, firstly, fine grid with more computational nodes are distributed is possible but this method could require a more computational effort. Thus a re-distribution of grid points especially at the boundary in the core region is needed to decrease error using the same grid number.

### **4.3 Benchmarking with the CARRE code**

A well-known 2-D mesh code for edge-divertor plasma, named CARRE [4], is chosen to benchmark the developed code with the same grid distributions. The reference equilibrium is chosen to be a double null configuration and

node number and grid distribution are also set to be the same in the entire regions. The conditions of input parameter are above as Table 4.1 and 4.2.

Figure 4.6 shows the total averaged quantities of deviation parameters which are cell orthogonality, radial flux deviation and standard deviation of  $\psi$ , computed in the double null configuration by vector following method and CARRE codes. A qualitative similarity in overall region is seen in both vector following method and CARRE code of mesh generation, especially, in Figure 4.6 (c) indicates the standard deviation of  $\psi$  is nearly same as order of minus four. However, the deviation levels in the private regions (region 2, 4) are relatively lower than the CARRE results.

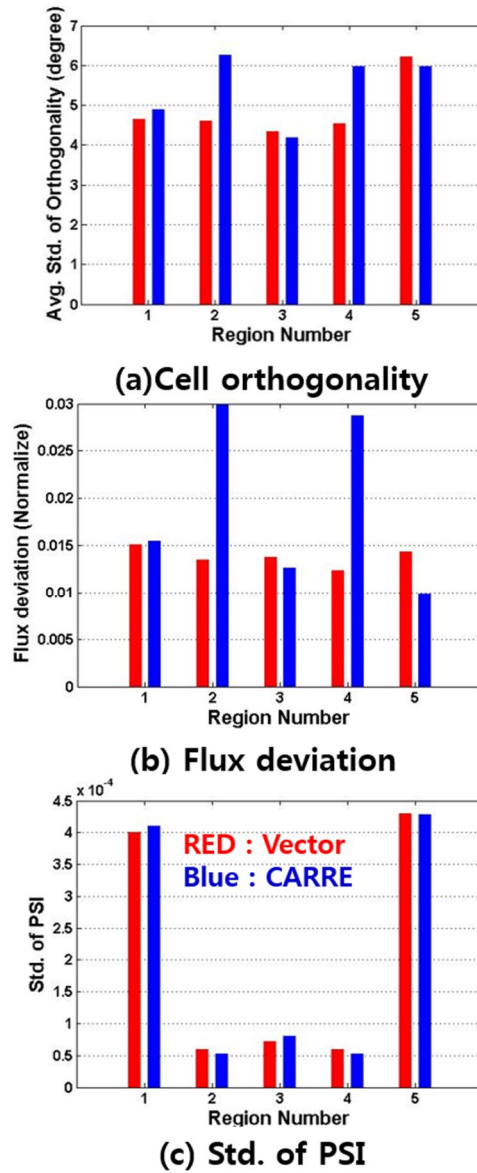


Figure 4.6 Comparison of the averaged quantity of deviation parameters from an ideal orthogonal mesh in the reference double null configuration, which are computed by vector following method(red) and CARRE(blue) code, respectively.

Such discrepancy is believed to result from the different treatment near divertor plates. In the vector following method, divertor constraint makes mesh polygon to be similar with divertor plates but bias of the CARRE code is the making the new flux surface to be similar to the one on the starting boundary [4]. Figure 4.7 shows the variations of deviation parameters at the private regions (region 2, 4). In view of radial scanning, most differences appear near the boundary surfaces like separatrix line and private region limits. Because the CARRE method is intended to make flux surfaces to be similar with separatrix line as possible, different field line shapes between two layers cause more deviations than vector following method. In the poloidal direction, the one peak point is investigated at the X-point but the other one also exists in the CARRE results. X-point peaking is the global tendency in the overall regions where orthogonal shape is impossible due to the large variation of contour lines. However, CARRE method also has peaked point near the outer divertor plate where the starting points of grid generations in the vector following method. In general, SOL-private regions appear large gradient value near the divertor plate like ion temperature and neutral density. So this big differences can affect the divertor simulations such as divertor heat load caused by heat flux and detachment zone from moving of high neutral area, which is possibility for MARFE at a vicinity of X-point [20].

The comparison results in core regions are also shown in Figure 4.8 because our mesh generator is intended to focus on the core region with time varying core equilibrium conditions.

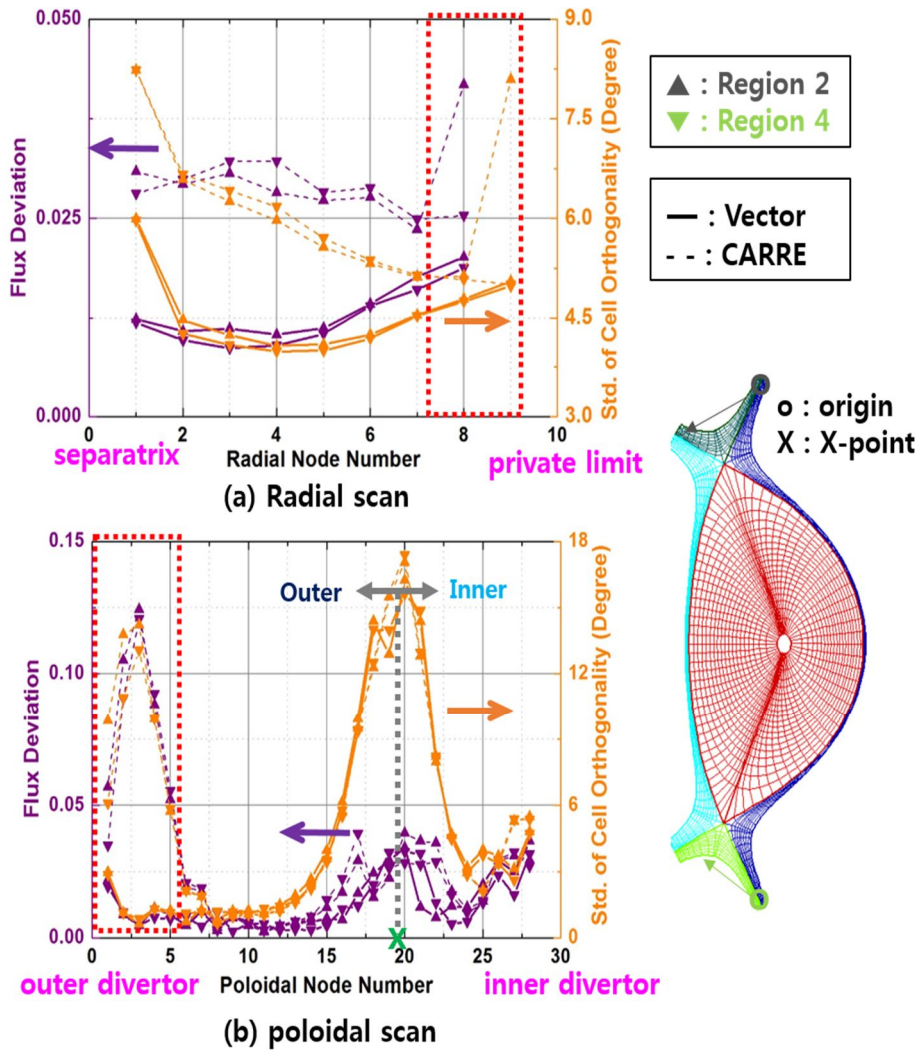


Figure 4.7 Variations of deviation parameters in the private regions (region 2, 4) along the (a) radial and (b) poloidal direction. Left axis indicates radial flux deviations and right one is cell orthogonality.

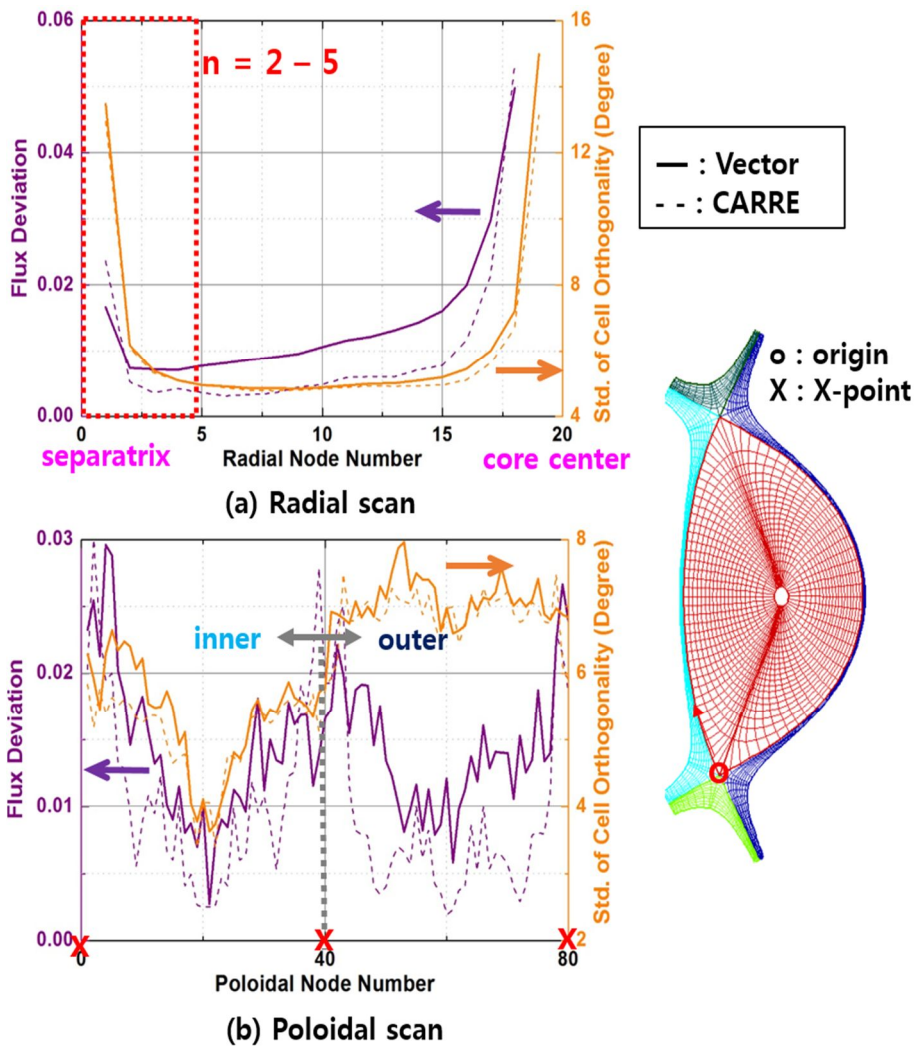


Figure 4.8 Variations of deviation parameters in the core region (region 5) along the (a) radial and (b) poloidal direction. Left axis indicates radial flux deviations and right one is cell orthogonality.

In comparison with two separatrix, the inner separatrix has lower deviations than the outer one. It is confirmed to large variation of contour line makes orthogonal mesh construction hard. The trend of radial variation is similar with Figure 4.8 (a) and the cell orthogonality between the two codes show nearly same results, though, radial flux deviation is somewhat different. In vector following method, less deviation is appear near the boundary but large deviation is observed in the middle area and the CARRE code is vice versa.

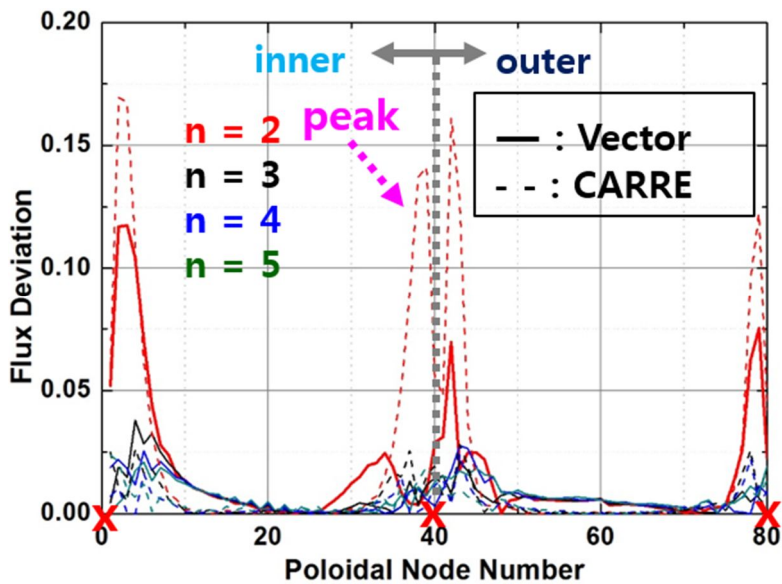


Figure 4.9 Poloidal variations of flux deviation in the core region (region 5) at the each flux surface in the vicinity of the edge region.  $n$  refers radial node number.

To more specific analysis near edge region, Figure 4.9 is plotted which is the expansion of the Figure 4.9 (a) from  $n = 2$  to  $n = 5$ . The most deviations occur at the  $n = 2$  surface where the most close to the separatrix line and vector following method seems to be less peak point than CARRE method at the X-point. This allows more accurate calculation is possible at the edge region when a gradient of the plasma is high at that area. In addition, an improvement of flux conservation more desirable for the overall simulation which includes interregional transport between the two different regions such as core-SOL transport. Because the edge region is close to the separatrix where boundary region for a distinction of confinement characteristics due to the magnetic topology, numerical error to the other regions can be diminished caused by reducing error near the boundary.

Figure 4.10 is the results for an error of a radial transport on separatrix lines. The vector following method is more proper for the transport than the CARRE method except the forth separatrix line. The detail graph of poloidal variation each separatrix line is presented in Figure 4.11. Figure 4.11 (a) shows highest difference appear at the outer divertor plates which is related to the distinction of constraint condition between the two codes and deviation at the core separatrix where degree of deviation is much higher than the divertor separatrix is more alleviated for using vector following method. In general, edge-SOL-private regions are normally not constant along poloidal direction and that means radial flux conservation is more important not to mix parallel and perpendicular transport for the accurate

calculation results. Therefore, calculation domain based on the vector following method gives a more precise domain for simulation of various boundary phenomena such as ELMs, MARFE and inward pinch of neutral particles [11].

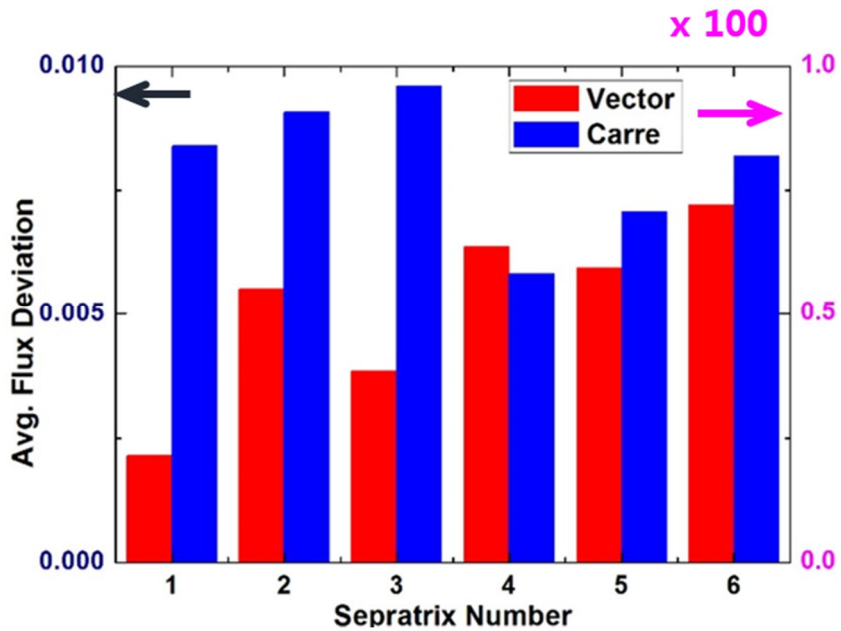


Figure 4.10 Comparison of the average value of flux deviation at each separatrix lines (1: upper right, 2: upper left, 3: lower right, 4: lower left, 5: outer core, 6: inner core) which are computed by the vector following method (red) and CARRE (blue) code, respectively. Left axis indicates the divertor separatrix (number = 1, 2, 3, 4) and right one indicates the core separatrix lines (number = 5, 6). The magnitude of right axis is more one hundred times than left axis.

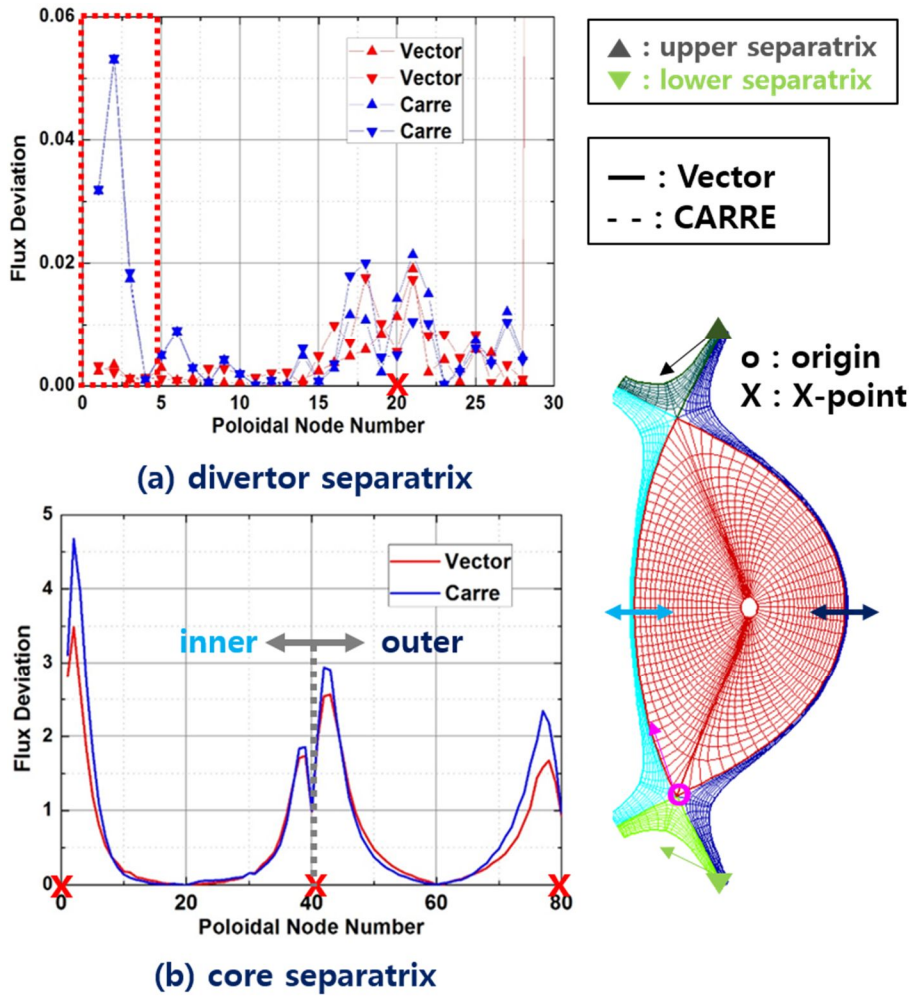


Figure 4.11 Radial flux deviations at each separatrix lines along the poloidal direction: (a) divertor separatrix and (b) core separatrix, which are computed by the vector following method (red) and CARRE (blue) code, respectively.

## **Chapter 5**

### **Automatic Non-uniform Grid Generation**

To apply the developed code in a core-edge coupled simulation, the grid in a core region must be reallocated automatically for representing time varying equilibrium. It is not helpful using passive distribution parameter for a next core mesh generation for a dynamic grid generation, so a direct mesh generation that adopts a plasma parameter in the transport solver is needed. As mentioned in chapter 3, adaptive core distribution parameters like ion temperature and 1-D equilibrium profile are useful as reference parameters for the next generation of mesh.

#### **5.1 Input profile for the core distributions**

##### **5.1.1 Stationary mode**

To adopt stationary mode, all average quantities in the plasma must change slowly in time and space. The distribution function becomes a Maxwellian in a time of the order of the collision time. In this condition, radial transport of the plasma mostly occur to the diffusion characteristic by random walk process. Therefore, if an ion temperature exists at each radial node number, radial grid can be reallocated to follow same gradient length

scale for the same temperature variation. In this thesis, the shape function is used for the profile making to test mesh configuration of stationary mode.

$$T_i(R) = (1 - R_n^\alpha)^\beta + T_{sep} \quad R_n = \frac{R - R_b}{R_a - R_b} \quad (5.1)$$

$R_a$  is a radial position at magnetic axis and  $R_b$  is a radial positions at the separatrix line and two points can be defined during field null seeking routine.  $T_{sep}$  is the ion temperature at the separatrix.

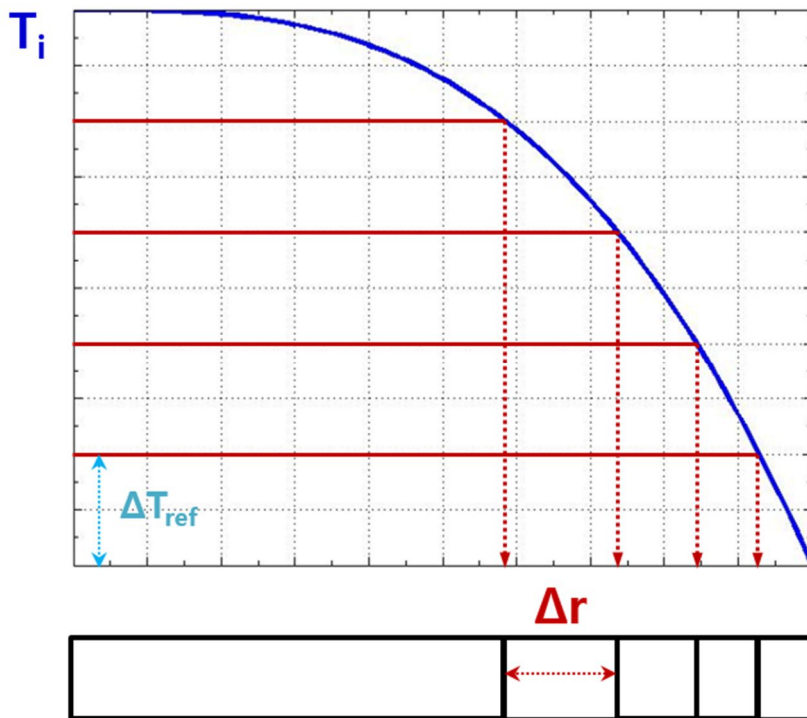


Figure 5.1 One dimensional radial ion temperature profile by the shape function in the core region for stationary mode

### 5.1.2 Subdomain mode

This mode uses 1-D equilibrium profile as a distribution parameter from an equilibrium solver to use additional codes. For more specific simulation at the edge region, distinction point between two sub domain in the core is selected to  $\rho_n = 0.95$  point. The distribution of subdomain mode is in Table 5.1. Normally, transport characteristics are highly varied at the pedestal area, so the main core distribution is led to the refinement in the vicinity of the distinction point. 1-D equilibrium give  $\psi_n$  and  $\rho_n$  which has the one to one correspondence in Figure 5.2.  $\psi_n$  is the normalized flux surface as described in equation (5.2).

$$\psi_n = \frac{\psi_n - \psi_a}{\psi_b - \psi_a} \quad (5.2)$$

Region	Node number ( $\chi, \phi$ )	Distribution
5	81 x 20	-
Main core	81 x 15	Non-uniform
Edge	81 x 5	Uniform

Table 5.1 Distribution of subdomain mode in the core region

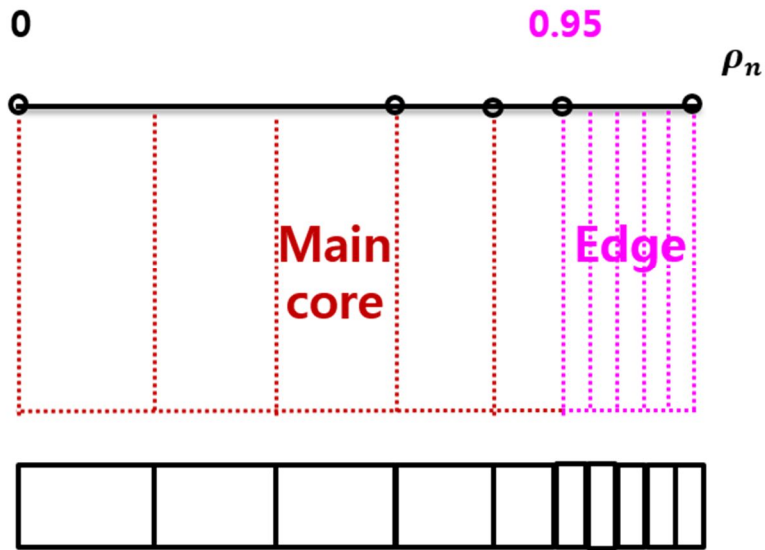


Figure 5.2 Radial distribution of the subdomain mode in the core region. Two subdomain is divided at the  $\rho_n = 0.95$ .

$\psi_a, \psi_b$  is the magnetic flux surface at the magnetic axis point and the plasma boundary, respectively.

## 5.2 Comparison with the reference distribution

As showed in Figure 5.3, core distribution is changed due to following the non-uniform distributions; refined grid at the edge, coarse grid at the core center, especially subdomain mode is the narrowest spacing near the separatrix line. This infers mesh quality factors in non-uniform distributions

are more improved at the edge region but deviations are more severe at core regions, a trade-off between refined grid and coarse grid in a finite grid number.

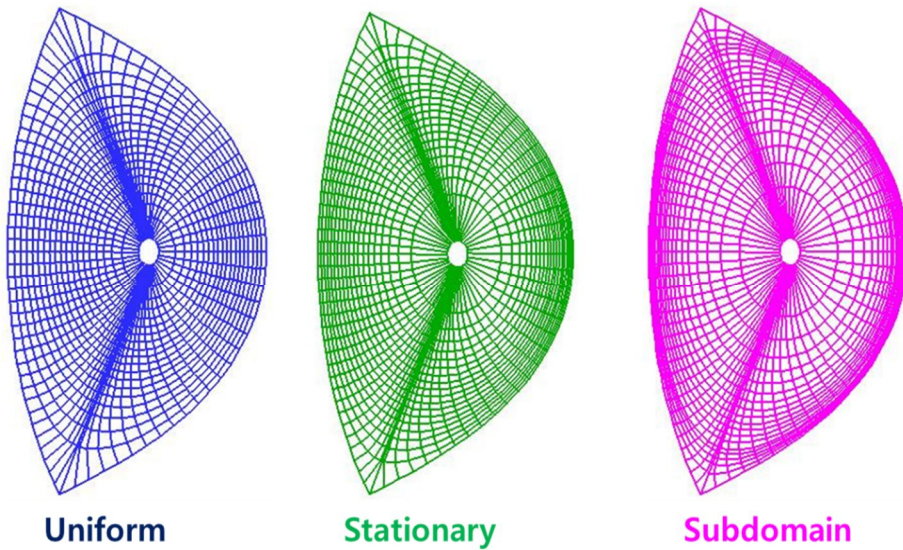


Figure 5.3 Core distribution shapes of various operation mode: uniform distribution (blue), stationary mode (green) and subdomain mode (magenta), respectively.

Figure 4.4 shows the most deviation is occur near the separatrix line so refined grid at the edge region makes mesh quality from  $n = 2$  to  $n = 4$  flux surfaces improved. Fig 5.4 shows averaged value from a region 1 to region 4 is exactly same both cell orthogonality and radial flux deviation because

distribution parameters are same except for the core region. But deviation factors in the core region (region 5) are slightly different each other due to the non-uniform distribution. In an edge transport barrier simulation, a central core grid distribution is less important than an edge region, so refined grids at the edge region are required in that case.

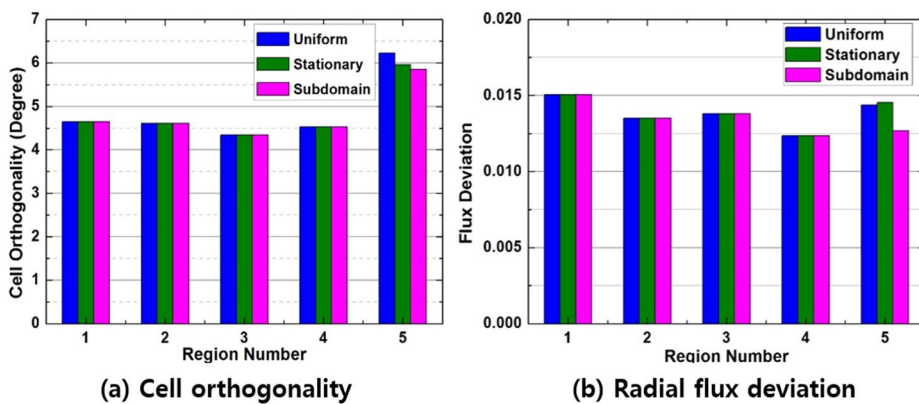


Figure 5.4 Comparison of the averaged quantity of deviation parameters: (a) cell orthogonality (b) radial flux deviation from an ideal orthogonal mesh in the various core distributions.

Figure 5.5 shows an X-point peaking of cell orthogonality and flux deviation are reduced at the edge region, in particular subdomain mode is the most alleviated operational mode in that case. Furthermore, radial transport at the separatrix lines ( $n = 1$ ) is highly improved due to the non-uniform distribution in the core region. Figure 5.6 indicates radial flux error is largely

reduced near the X-point branch. An average radial flux deviation in subdomain mode is about 11 times smaller than uniform distributions, which ensure boundary physics could be solved more accurately by the grid refinement.

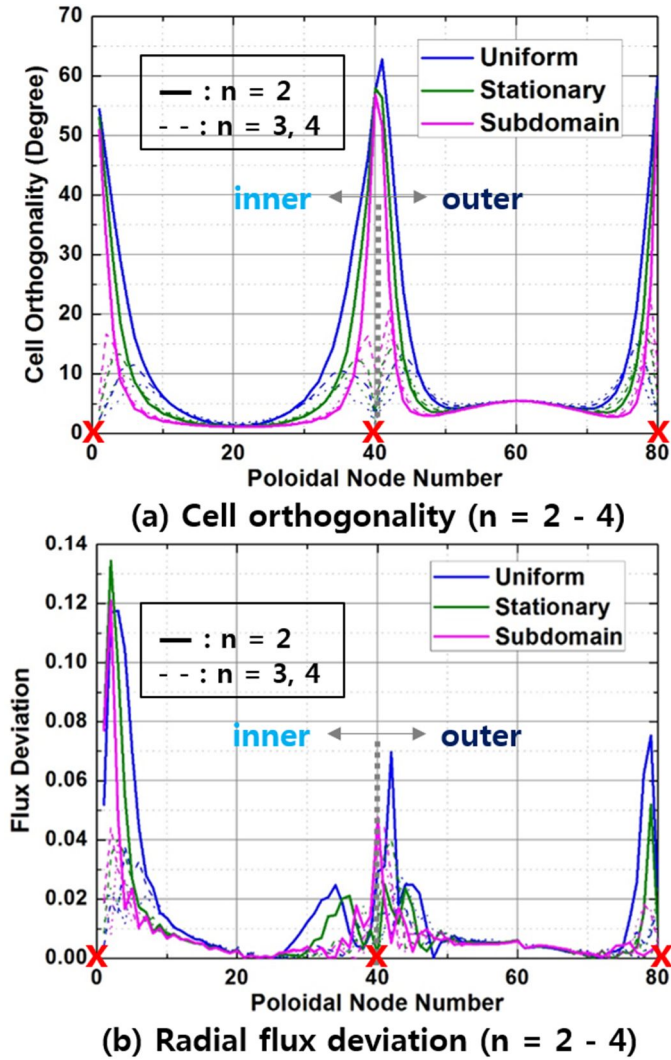
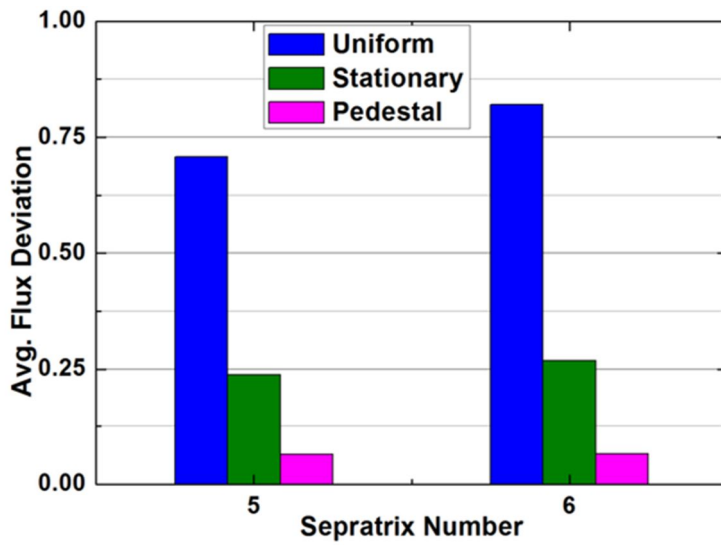
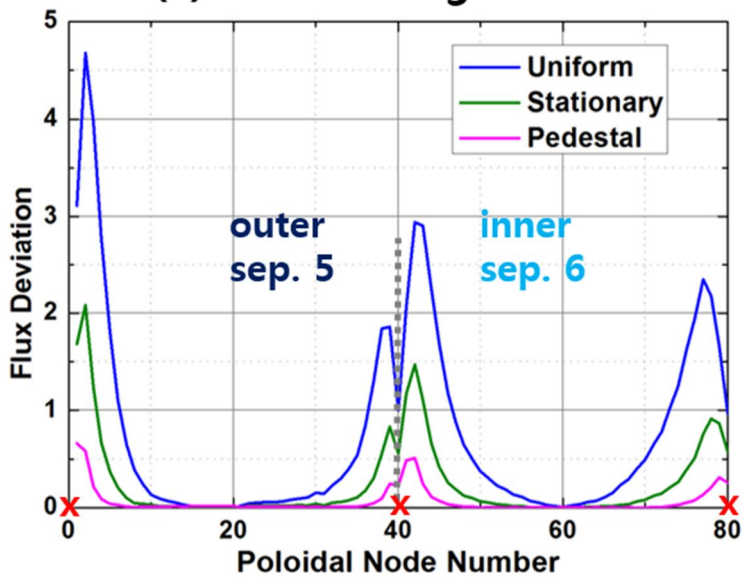


Figure 5.5 Poloidal variations of (a) cell orthogonality and (b) radial flux deviation in the core region (region 5) for the various core distributions at the each flux surface from  $n = 2$  to  $n = 4$ .  $n$  refers radial node number.



(a) Total average value



(b) Poloidal scan

Figure 5.6 Radial flux deviations at the core separatrix lines for the various core distributions: (a) total average value and (b) poloidal scan.

## Chapter 6

### Conclusions

A field aligned quasi-orthogonal structured mesh generator which can provide calculation region for the FVM discretization is developed using a vector following method based on a poloidal magnetic field line map. This code can generate a non-uniform grid automatically coincide with a specific simulation purpose. By coupling with the transport solver, the core distribution could be reallocated to represent a time varying equilibrium.

The developed code is tested for various KSTAR divertor configurations. The result confirms that rectangular structured meshes can be created well. This code is also verified with the CARRE code. For analyzing the mesh quality suitable for the FVM method, several evaluation factors are introduced to satisfy flux conservation criterion; field alignment, cell orthogonality, and radial flux error. In terms of deviation quantities, the field alignment is nearly the same between the two codes. However, cell orthogonality and radial flux error of the developed code is found to be more improved at private regions. This different results mainly comes from near the divertor region. Especially, the radial transport error crossing the separatrix lines is much relieved in the newly developed code than the CARRE code. This could be more desirable to simulate boundary phenomena such as MARFE, ELMs and so on.

Finally, quality of the non-uniform grids automatically generated by the code

is evaluated in two ways. One is generated by considering the ion Larmor radius; stationary mode and the other by considering local steep gradients appearing such as in transport barriers; subdomain mode. They are compared with a reference uniform core distribution case. The non-uniform distribution of two modes shows more refined grids near the edge region whereas coarser one in the core region. In particular, the highest refined grid is generated in the subdomain mode at the edge region due to the local steep gradient there. Both cell orthogonality and radial flux error is improved since deviation factors at the X-point is highly reduced. The radial transport error at the core separatrix lines is also largely alleviated, which is more suitable for analysis of the edge-SOL transport.

The developed vector following mesh generator in this thesis has some limitations in application. Plasma configurations is restricted for only divertor configuration. Also, boundary of the plasma is assumed to be fixed during the simulation which is not appropriate when applied to plasma conditions where the plasma shape is varying such as in the current ramp-up phase. However, this code can cover most important phases where the core-edge coupled phenomena plays a dominant role.

The newly developed code will be fully verified after coupling with a transport solver. The adaptive mesh with this code will be available for time-varying integrated transport modeling of different spatial scales. This newly developed mesh generator is envisaged to enhance core-edge-SOL simulations for analyzing various outstanding phenomena such as L-H transitions, ELMs, and MARFE.

## Bibliography

- [1] M Fichtmüller *et al.*, "Core-edge Coupling and the Effect of the Edge on Overall Plasma Performance," JET-P(98)69 (1999).
- [2] J.M. Park, "Integrated Simulation of Tokamak H-mode Operation by a Two-Dimensional Plasma Transport Code in Coupled Core-Edge Pedestal-SOL Region," Ph.D. Dissertation, Seoul National University (2005).
- [3] H. Seto and A. Fukuyama, "Formulation of Two-Dimensional Transport in Tokamak Plasmas for Integrated Analysis of Core and Edge Plasmas," *Contrib. Plasma Phys.*, **52**, No. 5-6 384 – 390 (2012).
- [4] R. Marchand and M. Dumbery, "CARRE: a quasi-orthogonal mesh generator for 2D edge plasma modeling," *Com. Phys. Com.*, **96**, 232-246 (1996).
- [5] R. Schneider *et al.*, "B2-EIRENE simulation of ASDEX and ASDEX-Upgrade scrape-off layer plasmas", *J. Nucl. Mater.*, 196-198 810 (1992).
- [6] T.D. Rognlien *et al.*, "A fully implicit, time dependent 2-D fluid code for modeling tokamak edge plasmas", *J. Nucl. Mater.*, 196-198 347 (1992).
- [7] X. Bonnina *et al.*, "The Two-Mesh Grid Refinement Method for the B2 Code," *Contrib. Plasma Phys.* **42**, (2002) 2-4, 175 (2002).
- [8] H.S. Han, "Ideal MHD Stability Analysis and Edge-Divertor Plasma Transport Simulation on Tokamak Hybrid Scenario Operation," Ph.D. Dissertation, Seoul National University (2011).
- [9] E. Havlíčková, "Fluid Model of Plasma and Computational Methods for Solution", WDS'06 Proceedings of Contributed Papers, Part III 180–186 (2006).

- [10] D.S. Kershaw, "Differencing of the Diffusion Equation in Lagrangian Hydrodynamic Codes," *J. Comput Phys.*, **39**, 375-395 (1981).
- [11] J.D. Callen *et al.*, "Analysis of pedestal plasma transport," *Nucl. Fusion* **50**, 064004 (23pp) (2010).
- [12] Yaoxin Zhang, Yafei Jia, "CCHE2D Mesh Generator and User's Manual (v 2.00)", Technical Report No. NCCHE-TR-2002-5 (2002).
- [13] ITER Physics Basis Editors, "Progress in ITER Physics Basis," *Nuclear Fusion*, **47**, S1 (2007).
- [14] G.S. Lee *et al.*, "The KSTAR project: An advanced steady state superconducting tokamak experiment," *Nucl. Fusion*, **40**, No. 3Y 575 (2000).
- [15] R.C. Grimm *et al.*, "Ideal MHD stability calculations in axisymmetric toroidal coordinate systems," *J. Comput Phys.*, **49**, 94-117 (1983)
- [16] J. L. Johnson *et al.*, "Numerical Determination of Axisymmetric Toroidal Magnetohydrodynamic Equilibria," *J. Compu. Phys.*, **32**, 212-234 (1979).
- [17] Yaoxin Zhang and Yafei Jia, "CCHE2D Mesh Generator and User's Manual - Version 2.6", Technical Report No. NCCHE-TR-2005-05 (2005).
- [18] W.X. Wang *et al.*, "Gyro-kinetic simulation of global turbulent transport properties in tokamak experiments," *Phys. Plasma*, **13**, 092505 (2006).
- [19] Y.M. Jeon, "Design of optimal position and shape controller based on perturbed equilibrium response model for tokamak plasmas," Ph.D. Dissertation, Seoul National University (2006).
- [20] C. S. Pitchery and P. C. Stangeby, "Experimental divertor physics", *Plasma Phys. Control. Fusion*, **39**, 779 (1997).

## 국문초록

플라즈마 평형은 플라즈마 수송에 따라 변하기 때문에 시간변화적 적응성의 그리드는 토카막 플라즈마의 다차원 시간종속적 수송 모델에서 요구된다. 그리고 다양한 다른 공간 스케일이 존재하는 통합 수송 모델링을 위해선 불균등한 적응성의 그리드 또한 필수적이다. 기존의 많은 메쉬 생성기들은 SOL-private 영역에 집중하여 적절한 2 차원 계산영역을 제공하기 위해 개발되었지만, 일반적으로 시간에 따라 고정된 그리드를 제공하며 이 메쉬가 새롭게 재생성 되지 않는다. 따라서 이러한 코드들은 전체 시뮬레이션에서 플라즈마 값들이 시간, 공간에 대해 변하는 상황에 적합하지 않기에 L-H 천이, ELMs 과 같은 현상의 전산모사를 위해선 지속적으로 그리드를 재 생성하는 것이 요구된다.

위의 이유로, 2 차원 토카막 노심 및 경계 영역의 통합 전산모사 수송 코드와 적합하게 결합할 수 있는 새로운 방법의 메쉬 생성기를 개발하였다. 이는 플라즈마 형상은 어느 정도 고정되어 있으며 내부의 평형이 바뀌는 조건에 활용된다.

개발된 메쉬는 토카막 내 자화된 플라즈마 조건에서 자기장의 평행 및 수직 방향의 비등방성 수송을 분리하여 해석하기 위해 쓰이는 유한적분법 (FVM)에 적용되도록 자기장에 정렬된 수직 모양의 구조화된 형상을 가지고 있다. 이를 위해 메쉬는 Single Null (SN)과 Double Null (DN) 디버터 형상에 적합하도록, 주어진 플라즈마 평형 정보를 통해 얻은 폴로이달 자기장 방향장에 기반하여 수직하게 생성된다. 또한 수송 코드와의 직접적인 결합을 통해 플라즈마 현상 해석을 위한 다양한 전산모사 목적에 맞는 적합한 계산 영역을 제공하는 최적화된 그리드 분배를 제공함으로써 유연성을 확보하였다. 이 때 그리드 분배는 정성적, 국부적 현상 모두 해석하기 위해 몇 가지 공간 스케일에 맞춰 균등 하지 않게 이루어진다.

일반적으로 플라즈마 수송 방정식과 차분화 방정식 사이의 좌표변환 식이 주어지지 않기 때문에 메쉬 생성은 보간법과 같은 대수적인 추정에 의해 이루어지게 된다. 이런 조건에서의 메쉬 생성을 위해 플로이달 자기장 방향장의 정보를 통해 얻은 방향 벡터를 따라가며 원하는 위치를 찾는 벡터 추적 방법론을 도입하였다. 이 방법은 메쉬 생성의 전체 과정에 널리 사용되며, 임의의 플라즈마 형상에 대해 정확한 직사각형 모양의 메쉬 형상을 제공할 수 있다.

위의 방법론을 적용하여 새롭게 개발된 메쉬 생성기는 세 가지 방법으로 검증하였다. 가장 먼저 TES 코드 결과를 평형 값으로 하여 KSTAR 형상의 메쉬를 생성하였고, FVM 에서의 플럭스 보존 조건에 기반하여 몇 가지 메쉬 평가 값들을 새롭게 정의하여 생성된 메쉬를 평가하였다.

그리고 이런 메쉬 평가 값들을 기존의 메쉬 생성코드인 CARRE 코드와 비교하여 개발된 코드를 검증하였다. 그 결과 전반적인 수치 값들은 서로 비슷한 모습을 보였으나, 두 코드의 경계 값 부근의 제한조건 차이로 인해 private region 에서 벡터추적법이 CARRE 코드에 비해 보다 향상된 평가 값을 갖는 것을 확인하였다. 또한 separatrix 에서의 반경 방향 수송 오차가 벡터추적법에서 보다 더 작게 나타났으며, 이는 MARFE, ELMs 과 같은 플라즈마 경계영역의 물리현상을 모사하는데 있어 보다 적합할 수 있다.

마지막으로 비 등간격 그리드 생성 결과를 평가하였다. 노심영역의 비 등간격 그리드의 생성은 이온 Lamor 반지름을 고려한 방법과 수송 장벽과 같은 급격한 기울기를 고려한 방법 두 가지로 나눌 수 있다. 이 두 방법을 등간격 그리드 분포와 비교하였다. 그 결과 작은 Lamor 반지름 및 급격한 기울기 때문에 경계 영역에서 그리드가 조밀하게 형성되었으며 노심 안쪽에서는 넓은 그리드 간격의 메쉬가 생성되었다. 경계 영역에서 나타나는 이러한 그리드

간격 차이는 separatrix 에서의 경계-SOL 영역 수송에 있어 더 적합하다.

따라서 본 논문에서 개발된 자기장 추적 메쉬 생성기는 장차 수송 코드와 직접 결합함으로써 플라즈마 평형 재생성에 맞게 시간에 따른 재 구축이 가능한 적응성의 그리드로 발전될 수 있을 것이다. 그리고 이는 노심-경계-SOL 통합 전산모사에 활용될 수 있다.

주요어: 직사각형 메쉬, 벡터 추적법, 자동적 비 등간격 그리드 생성, 2 차원 토카막 수송, 유한적분법 차분화, 메쉬 평가, 전산 코드

학 번: 2012-20993